Synthesis, Structure and Some Properties of $ThCr_2Si_2$ Type Compounds: $AeCo_2Ge_2$ (Ae=Ca,Sr) and ACo_2As_2 (A=K,Ba)

A Thesis Presented to

the Faculty of the Department of Chemistry

University of Houston

In Partial Fulfillment

of the Requirements for the Degree

Masters of Science

By

Lekh Raj Aryal

December 2013

Synthesis, Structure and Some Properties of $ThCr_2Si_2$ Type Compounds: $AeCo_2Ge_2$ (Ae=Ca,Sr) and ACo_2As_2 (A=K,Ba)

Lekh Raj Aryal

APPROVED:

Dr. Arnold M. Guloy, Chairman

Dr. Allan Jacobson

Dr. Ding-Shyue (Jerry) Yang

Dr. Alexander P. Litvinchuk

Dean, College of Natural Sciences and Mathematics

Synthesis, Structure and Some Properties of $ThCr_2Si_2$ Type Compounds: $AeCo_2Ge_2$ (Ae=Ca,Sr) and ACo_2As_2 (A=K,Ba)

An Abstract of a Thesis

Presented to

the Faculty of the Department of Chemistry

University of Houston

In Partial Fulfillment

of the Requirements for the Degree

Masters of Science

By

Lekh Raj Aryal

December 2013

ABSTRACT

This research was motivated by the variety of electronic and magnetic properties that ternary intermetallic compounds, AT_2X_2 (A= alkali/alkaline earth metals, T = transition metal and X = post-transition metal) exhibit. These polar intermetallics crystallize in the ubiquitous $ThCr_2Si_2$ structure type (space group I4/mmm) or derivatives of it. In this context, the ternary cobalt germanides: $CaCo_2Ge_2$ and $SrCo_2Ge_2$, and arsenides: KCo_2As_2 and $BaCo_2As_2$, were synthesized and characterized. The ternary cobalt germanides were prepared from the elements by arc melting techniques, and characterized by means of single crystal and powder X-ray diffraction. The ternary arsenides were synthesized from the high-temperature reactions of the respective active metals (K, Ba) with pre-reacted binary CoAs within welded Nb containers. The ternary arsenides were characterized by means of powder X-ray diffraction. $CaCo_2Ge_2$ and KCo_2As_2 were found to be weakly ferromagnetic while $BaCo_2As_2$ was pauli-paramagnetic. Finally, the solid solubility of $BaCo_2As_2$ and KCo_2As_2, to prepare $Ba_{(x)}K_{(1-x)}Co_2As_2$, was investigated by the powder X-ray diffraction. The crystal chemistry and the physical properties of the ternary compounds are discussed.

Acknowlegement

I wish to express my sincerest appreciation to my advisor, Dr. Arnold M. Guloy, for his guidance and support during my graduate research. I would also like to thank Dr. Berd Lorenz for the physical measurements and invaluable suggestions. My appreciation also goes to my other committee members: Dr. Allan Jacobson, Dr. Ding-Shyue (Jerry) Yang, and Dr. Alexander P. Litvinchuk.

I am also indebted to Dr. Zhongjia Tang for helpful discussions and his assistance during the research work.

Thanks to all the members of the Guloy's group for their help and encouragements.

Table of contents

Chapter 1

Literature Review

1.1 Introduction

This work is motivated by the search for new classes of layered 122 intermetallic superconductors by using a rational intergrowth building block multilayer approach and at the same time explores the ways to induce the superconductivity of layered intermetallics by tuning their electronic properties [1-4].

It was in 1911 that superconductivity was first discovered by H. K. Onnes[5] several years after the discovery of liquid helium, while studying the resistance of solid mercury at cryogenic temperatures. He found that at 4.2 K the resistance of a solid mercury wire immersed in liquid helium suddenly disappeared and hence exhibited zero resistance to electric current. In the next three years, he found that tin and lead also became superconductors at the temperatures of ~3.8 K and ~7K respectively. And the superconductivity could be destroyed by applying the external magnetic field (H) greater than some critical field (Hc). Furthermore, in 1933 German physicists Meissner and Ochsenfeld found the expulsion of applied magnetic fields by superconductors during its transition to superconducting state[6]. This now has come to be known as Meissner Effect.

A superconductor is a material that has two characteristic properties: zero electrical resistance and perfect diamagnetism. There is complete disappearance of electrical resistance in solids when they are cooled below a characteristic temperature. This temperature is called transition temperature or critical temperature, represented by

Tc. The property of zero resistance and high current have a high impact on electric power transmission and also enable much smaller or powerful magnets for motors, generators, energy storage, medical equipment and industrial separations. Currently, more than 30 of the elements become superconducting when they are cooled from their normal state.[7-8] These are shown in the periodic table below. Superconductivity can be observed in the conventional metals, alloys, oxides and other inorganic and organic molecules.

1.2 Intermetallics and their Classification

Intermetallics can be defined as solid phases composed of metals and semimetals with narrow range in the stoichiometry. More than 20,000 alloys and compounds are known in the solid state field nowadays [9-10] so it is important to classify these compounds based on crystal structures and bonding in a systematic way. Based on the following, a set of rules were postulated by Hume-Rothery:[11] a) differences in electronegativity between constituent atoms; b) atomic size factor effects; c) the tendency of s-p metals and transition metals to fill their s-p and d shells; d) electron concentration; and e) orbital restrictions related to the symmetry conditions for orbital hybridization. W. B. Pearson using the bond orders calculated the electron concentrations around each type of atom and classified intermetallics into five different groups according to their building principles and physical properties.[12-14]

1) Intermetallics that exhibit geometrical closed packing: These include most of the intermetallic phases. They are characterized by a negative volume of formation compared to the sum of the elemental atomic volumes.

2) Intermetallics where the band structure energy is a large fraction of the total energy. Structural changes are observed for certain values of electron concentration per atom.

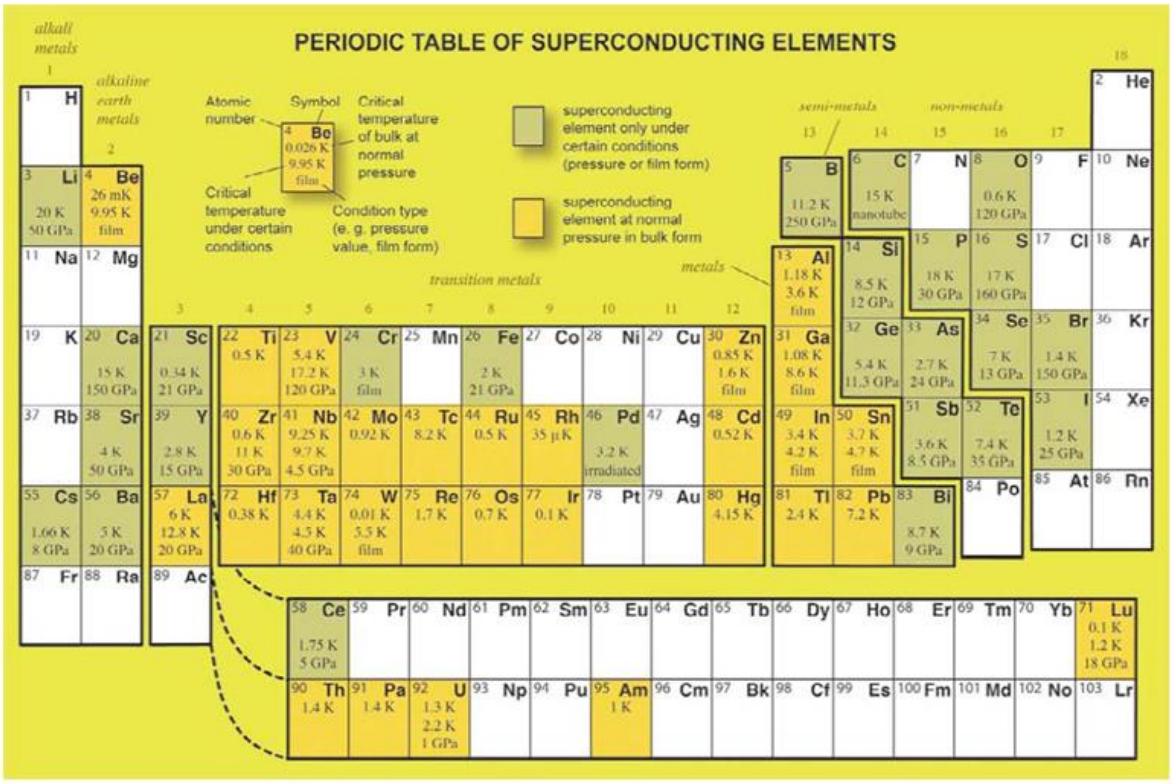

Figure 1.1: Periodic table of Superconducting elements [7].

3) Valence compound compositions in which chemical valence rules are satisfied. This group includes the normal valence compounds such as Mg_2Sn and the compounds that obey the Zintl concept like NaPb.

4) Intermetallics with a framework structure: In these compounds, all atoms form a common framework in which the distances to the nearest neighbors adhere to Pauling's formula:[15,16]

$$dn = d1 - 0.3logn$$

n: bond order (n = valence/coordination number); d_1: the single-bond length.

This equation relates bond distances, d, to the bond strength measured in terms of the number of valence electrons per ligand. No rules for valence or valence concentration are satisfied. Examples are MX_2 and MX'X" phases with Cu_2Sb structure type.

5) Intermetallics with hybrid framework structure: Examples of these compounds include $BaAl_4$ or $ThCr_2Si_2$ where atoms on certain sites form a partial framework and the remaining are accommodated in the large voids according to the geometrical packing principles.

The Zintl concept is proven to be an effective tool in describing the structural properties and chemical bonding of s-p intermetallic compounds along the borderline between metals and non-metals.[17-21] Zintl phases act as a bridge between classical valence compounds and normal intermetallic compounds. After investigating binary intermetallic compounds, E. Zintl proposed the idea, in which one component was far more electropositive than the other,[22,23] Zintl observed significant contractions in the unit cell volumes which did not follow the Hume-Rothery rule.[24] Rather than evaluate a total

valence electron concentration (VEC), Zintl proposed an idea that electron transfer from the electropositive component to the electronegative component.[25] Here, covalent polyanionic networks are formed if the electrons received from the electropositive atoms do not fulfill the octet requirements of the electronegative elements. This is how the terms Zintl phases and Zintl concept were introduced. Zintl defined a class of compounds that forms a connection between intermetallic phases, on the one hand, and valence compounds on the other. Mooser and Pearson[26] as well as Klemm and Busmann[27-30] correlated the general 8-N rule with the possible anionic substructures in normal valence compounds A_aX_x. The Zintl-Klemm- Busmann concept or Zintl-Klemm concept states: "In Zintl's idea the formally negatively charged atoms that possess the same electron number as the neutral atoms of the next group elements, form polyanions with similar structures to the corresponding elements."[31]

R. Nesper proposed a precise definition of Zintl phase, thus well differentiating it from other well-known groups of compounds, such as insulators and typical intermetallic phases.[32] He stated that Zintl phases should exhibit the following characteristics:

1. There is a well-defined relationship between the chemical structure and electronic structure of a Zintl phase. For most of these compounds short interatomic X-X contacts represent two center two electrons bonds and the octet rule is fulfilled for both isolated cations and polyanions. The charged $[X(aeA/x)^-]$ unit in AaXx can be considered as a pseudo-atom or pseudo-element proposed by W. Klemm[33-36] where eA is the number of valence electrons for atoms A.

2. Zintl phases are semiconductors. The band gap limit is taken at 2.0 eV.

3. Zintl phases are mostly diamagnetic, but can be paramagnetic like O_2.

1																	18
H	2											13	14	15	16	17	He
Li	Be											B	C	N	O	F	Ne
Na	Mg	3	4	5	6	7	8	9	10	11	12	Al	Si	P	S	Cl	Ar
K	Ca	Sc	Ti	V	Cr	Mn	Fe	Co	Ni	Cu	Zn	Ga	Ge	As	Se	Br	Kr
Rb	Sr	Y	Zr	Nb	Mo	Tc	Ru	Rh	Pd	Ag	Cd	In	Sn	Sb	Te	I	Xe
Cs	Ba	La	Hf	Ta	W	Re	Os	Ir	Pt	Au	Hg	Tl	Pb	Bi	Po	At	Rn
Fr	Ra	Ac															

Table 1.1: Periodic table of the elements showing the border between metals and metametals. In the gray zone are the elements considered as metametals defined by Klemm. The heavy line is the so-called Zintl border, which separates group 13 from 14 elements named by Laves.[37]

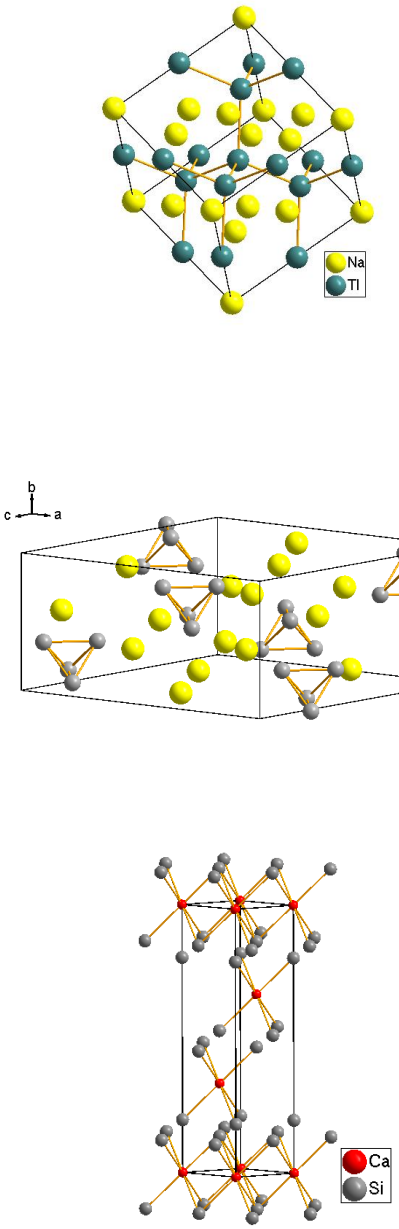

Figure 1.3a: NaTl crystal structure; Na:yellow and Tl:green spheres **b**: NaSi crystal structure; Na: yellow and Si: grey spheres and **c**: $CaSi_2$ crystal structure; Ca: red and Si: grey spheres.

The constituents of Zintl phases can be grouped as metals A and metametals X. Table 1.2 shows the border between nonmetallic elements and the typical metals. The compounds which are formed with elements to the right of the Zintl border are salt-like compounds and they have a defined chemical composition and crystal structures, whereas the metallic phases formed with elements to the left of the Zintl border have considerable phase-widths and crystallize in typical alloy structure types. The classical example of Zintl phase is NaTl. Its structure (Figure 1.3a) is formed from two interpenetrating diamond lattices (Na and Tl). Each Tl atom is tetrahedrally coordinated to Tl atoms. Zintl considered NaTl as polar $Na^{+}Tl^{-}$ with Tl^{-} present not as a simple monoanion but as an extended 3D anionic framework, analogous with group 14 elements, C and Si. According to this principle, NaSi can be described as Na_4Si_4 ($4Na^{+} + Si^{4-}$) with silicon (Figure 1.3 b) forming discrete tetrahedral units Si_4^{4-} , isoelectronic with the P_4 and AS_4 in white phosphorus and yellow arsenic, respectively. In $CaSi_2$ (Figure 1.3c), the anionic substructure (Si_2^{2-}) is a puckered layer of fused hexagonal rings as found in black phosphorus and grey arsenic.

The empirical boundary between group 13 and group 14 elements well signifies the limitation of the Zintl concept. The violations can be seen in group 14 and 15 elements so it can be said that the Zintl border is not absolute. Along the Zintl border, complex intermetallics with the combination of alkali metals or alkaline-earth or rare-earth metals with late- and post transition metals are called polar intermetallics. At the Zintl border between Zintl phases and intermetallics, typical properties of Zintl phases diminish and metallic conductivity appears, thus, there is the smooth transition in chemical bonding and electronic properties from electron-precise Zintl phases to nearly-

free-electron intermetallics. This opens up an area to search for interesting and new structural chemistry of intermetallics with novel electronic properties like thermoelectricity, magnetism and superconductivity.

1.3 Intermetallic Superconductors

Before the discovery of cuprate superconductors in 1986, research on intermetallic superconductors was mainly through B. T. Matthias's efforts.[38-39] Table 1.2 lists some interesting examples of intermetallic superconductors,[40] of which the important family of A15 intermetallic Nb_3X (X=Ge, Ga, Sn, Al etc) superconductors have relatively high Tc and high critical field (with highest Tc of 23.2K) in Nb_3Ge.

Figure 1.4 shows the crystal structure of the A15 family of compounds. It is based on the simple body-centered packing of the metalloid element (X) with Nb chains along the faces of the cubic cell. A15 Superconductors are found for Nb-, Ta-, and V- based compounds, and their Tc's generally found between 15 and 20 K. The other kinds of superconductors are the layered quaternary lanthanide nickel borocarbides and boronitrides that were discovered in 1994.[41-42] These exhibit higher Tc's than the ternary metal borides which were previously studied.[43-44] These types of intermetallics exhibit layered strutures of the general type $(LnX)_n(NiB_2)$ where Ln=lanthanide, particularly the nonmagnetic LaIII or LuIII; X=C or N; n=1,2 or 3) and these adopt the $LuNi_2B_2C$ structure type. In this type of structure, layers of rock salt like slabs of LuC are alternately stacked with Ni_2B_2 layers having the tetrahedrally-coordinated NiB_4 units (Figure 1.5).

Discovery of superconductivity in MgB_2 a Zintl phase, with the critical temperature of 39 K[45] had been of prime importance because of its honeycomb layers

Compounds	Crystal structure	Structure Type	Tc(K)
Nb_3Ge	Cubic	A15	23.2
NbN	Cubic	B-1	17.3
BiNi	Hexagonal	B-8	4.2
Au_5Ba	Hexagonal	D-2	0.7
PdTe	Rhombohedral	C-6	1.5
$PbMo_6S_8$	Rhombohedral	Mo_3Se_4	15.2
$ScRu_4B_4$	Tetragonal	$LuRu_4B_4$	7.2
$LaRh_3Si_5$	Orthorhombic	$U_2Co_3Si_5$	4.4

Table 1.2: Some examples of intermetallic superconductors.

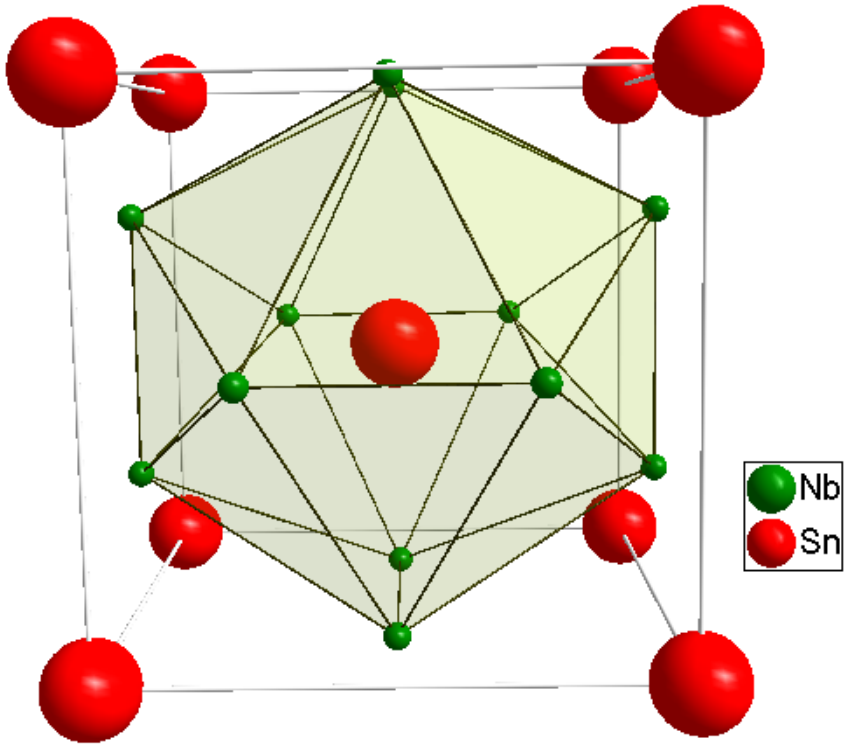

Figure 1.4: Nb_3Sn structure: Nb: green Sn: red, Nb-Sn bonds are not shown in the picture.

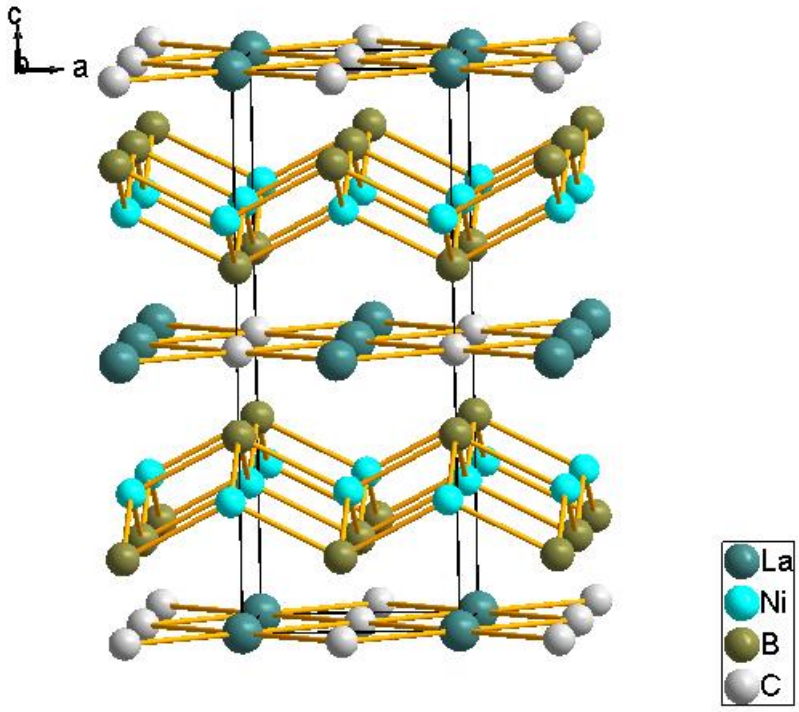

Figure 1.5: Crystal structure of $LaNi_2B_2C$. La:bluish green; Ni:Green; B:greyinsh green; C: white spheres.

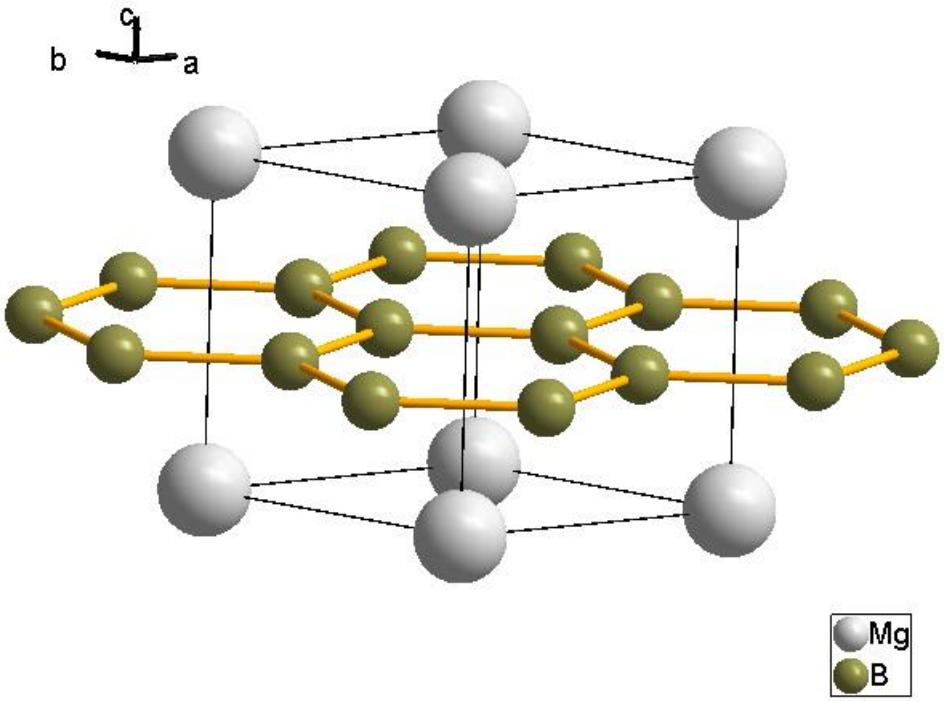

Figure 1.6: Crystal Structure of MgB_2. Mg represented as white spheres and B as grey spheres.

structure, which is analogous to graphite. The magnesium atoms, sandwiched between the graphite-like B sheets form layered triangular arrays. And MgB_2 can be regarded as graphite intercalation compounds with the magnesium atoms being intercalated between boron layers. Despite the B_2^{2-} being isoelectronic with graphite, it is quite metallic. Here phonons with electrons play a significant role in pairing mechanism thus can be considered as the ultimate electron-phonon coupled superconductor.[46-47]

After the discovery of MgB_2, another intermetallic compound superconductor, $MgCNi_3$ with Tc = 8K, was found.[48] This material is interest due to its simple perovskite structure (Mg in Ca sites, C in Ti sites and Ni in O as compared to the familiar perovskite $CaTiO_3$) and nickel-rich composition that usually results in magnetism. The Tc increases with increase in x in MgC_xNi_3, while it decreases with the Ni site doped with other metals such as Co, Fe, Mn, and Cu. It also shows the increase in Tc with the increase in external pressure. Because of superconductivity arising from a ferromagnetic state, it is believed to be due to the presence of relatively localized nickel states at the Fermi level. Nevertheless, a clear picture between magnetism and superconductivity has not been completely established for this compound.

The discovery of superconductivity in another type of intermetallics such as $UGe_{2,}$[49] $ZrZn_{2,}$[50] and URhGe[51] revived the interest because of the coexistence of ferromagnetism and superconductivity within a narrow temperature range. The d-electron compound containing non-magnetic metals, $ZrZn_{2,}$ exhibits weak ferromagnetism with a small ordered magnetic moment, and a Curie temperature of 28K. While it is ferromagnetic, it undergoes a superconducting transition at 0.3 K. After applying a modest pressure, both ferromagnetism and superconductivity vanish simultaneously. This

indicates that superconductivity and magnetism are coupled in this type of superconductor.

There are other types of unconventional intermetallic superconductors called heavy fermion superconductors. Heavy fermion superconductors can be classified into two types based on their structure: [52]

a) Ternary transition metal carbides, borides and silicides containing f-block metals exhibiting stable multiple oxidation states such as Cerium in $CeCu_2Si_2$ [53] and $CeCoIn_5$ [54] or uranium in URu_2Si_2 [55] and U_2PtC_2 [56].

b) The binary alloys that contain multiple oxidation state actinides (particularly uranium) and nonactinide polyhedral clusters such as $Pt_{6/2}$ octahedra in UPt_3. [57]

Even though the transition temperatures in the heavy fermion superconductors are low (less than 2-3K), these systems are of interest in studying the fundamental mechanisms of superconductivity in strongly correlated system. The behavior of heavy fermion is based on the two unique characteristics:

1) The large values of the electronic specific heat coefficient (Cp/T) at Tc, in the order of a few hundreds to even thousands mJ/mol-K^2. These indicate that heavy quasiparticles participate in the superconducting pairing.

2) Competition or interplay, coexistence or coupling of the magnetic and superconducting order parameter exists in heavy fermions.

1.4 Iron Based Superconductors

In the recent years, superconductivity was discovered in several more classes of compounds containing tetrahedral iron pnictide or chalcogenide layers – some of which had been known for a long time, and others synthesized for the first time. In addition to

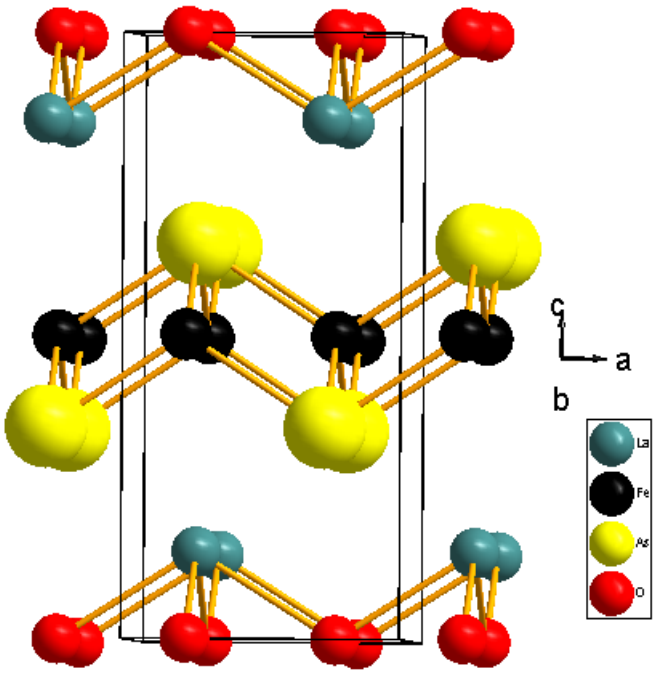

Figure 1.7: Crystal Structure of LaFeAsO. These form two layered structures namely LaO layer and FeAs layer. La, Fe, As and O represented as blue, black, yellow and red spheres.

the 1111- (the rare earth iron arsenide oxides $LaFeAsO_{1-x}F_x$ with transition temperature up to 26 K)[58] and 122-classes of iron arsenides, superconductivity is known to exist in the so-called 111-phases (for example LiFeAs[59-61] with Tc = 18K, $Na_{1-x}Li_xFeAs$ Tc, max = 25 K. Substitution of lanthanum by other rare earth metals Ce, Pr, Sm and Nd raises the superconducting transition temperature to 55K, which is the highest Tc except for the high Tc cuprates.[62-68]

High-temperature superconductors show features such as a layered structure, atomic substructures, strong electron-electron interaction, instabilities, and magnetic fluctuations. These all might be the factors in the occurrence of high-temperature superconductivity. In the equiatomic quaternary layered compounds ROTPn (R=rare earth elements, T=transition metal, Pn=pnictogen) as shown in the Figure 1.8 that adopts the ZrCuSiAs structure type, there are two layered substructures, viz, the the RO layers and the alternating tetrahedrally coordinated TPn layers.

TPn layeres are expected to form active block for the charge carriers to flow and the RO-layers make up the charge reservoir blocks that inject charge carriers into the block maintaining the maximum layer integrity of the TPn layers as in the cuprate high temperature suprerconductors. Though there are differences between the ROTPn and the cuprates, T is tetrahedrally coordinated with four Pn atoms in ROTPn and while Cu atoms are coordinated by four O atoms to form a square lane in the cuprates. Intensive researches are underway to raise their Tc, and to open the underlying mechanism for superconductivity in R(O,F)FeAs. In the same way that doping in oxypnictides compounds produce critical temperature to go as high as 55K, careful study in oxygen

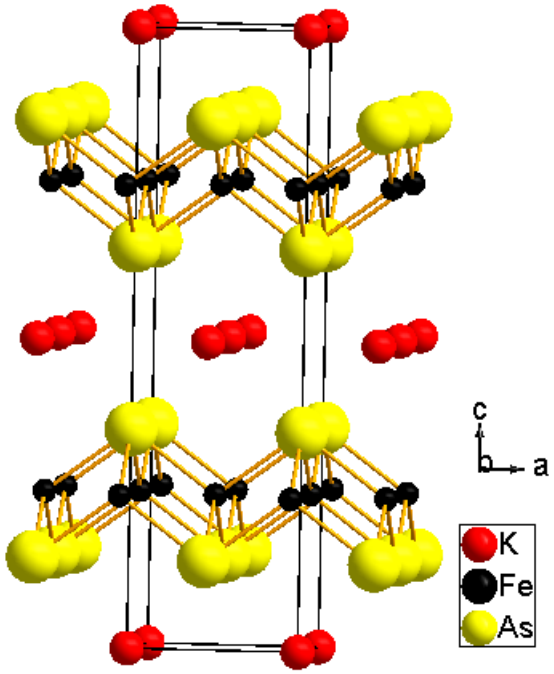

Figure 1.8: Crystal Structure of KFe_2As_2. Fe-As forms the layers and in between these layers, cation K is occupied. K, Fe and As are represented as red, black and yellow spheres.

free compounds with chemically different structures, but with similar charge carrier layers result in the AFe_2As_2[69,70] and $AeFe_2As_2$[71,72] compounds as illustrated in the Figure 1.8 that are crystallized in the tetragonal crystal system with space group I4/mmm (Space group No 139). The compounds belong to the well-known $ThCr_2Si_2$ structure type, with alkali metal or alkaline earth metal in place of Th, Co in place of Cr and As or Ge in place of Si. More than 700 compounds of AM_2X_2 have been reported to adopt the $ThCr_2Si_2$ structure type.[73] Here, A corresponds to an alkaline earth or lanthanide element, M is a transition metal and X comes from group 13, 14 or 15 elements.

Similarly, from Fe to Co with the increase in an electron, the Co_2As_2 layers that existed in the ACo_2As_2 (A=K) and $AeCo_2As_2$ (Ae=Ba) compounds drew a lot of attention. The Co_2As_2 layers in these compounds are separated with alkali or alkaline earth metal layers. What different properties will these compounds have compared to Fe_2As_2 compounds? As we know, in the large family of $ThCr_2Si_2$ type compounds, superconductivity was observed at temperatures below 5K, as in $LaIr_2Ge_2$[74-75], $LaRu_2P_2$,[76] $BaNi_2P_2$,[77] even though closely related rare earth borocarbides are known for Tcs up to 26K in YPd_2B_2C.[78] Does superconductivity occur in these compounds? Or on the various doped samples in these systems? With this in mind, we attempt to synthesize and investigate the properties of these alkali and alkaline earth ACo_2As_2 and $AeCo_2As_2$ system. Here, the synthesis, structure and physical properties of these compounds are reported.

References

(1) Guloy, A. M.; Goodey, J. *Condens. Matter News* 1**998**, *7*, 24-31.

(2) Brock, S. L.; Kauzlarich, S. M. *J. Alloys Compd.* **1996**, *241*, 82-88.

(3) Ozawa, T. C; Kauzlarich, S. M.; Bieringer, M.; Wiebe, C. R.; Greedan, J. E.; Gardner, J. S. *Chem. Mater.* **2001**, *13*, 973-980.

(4) Cava, R. J.; Zandbergen, H. W.; Krajewski, J. J.; Siegrist, T.; Hwang, H. Y.; Batlogg, B.J. *Solid State Chem.* **1997**, *129*, 250-256.

(5) Onnes, H. K. *Commun. Phys. Lab. Univ. Leiden.* **1911**, *12*, 120.

(6) Meissner, W.; Ochsenfeld, R.; Heidenreich, F. *Zeitschrift fuer die Gesamte Kaelte-Industrie* **1934**, *41*, 125-130.

(7) Buzea, C; Robbie, K. *Supercond. Sci. Technol.* **2005**, *18*, R1-R8.

(8) Geballe, T. H.; Matthias, B. T. *Annu. Rev. Phys. Chem.* **1963**, *14*, 141-160.

(9) Villars, P.; Calvert, L. D. *Pearson's Handbook of Crystallographic Data forIntermetallic Phases;* Second Edition ed., 1997.

(10) Pearson, W. *The crystal chemistry and physics of metals and alloys*, 1972.

(11) Hume-Rothery, W. *J. Inst. Met.* **1926**, *313*.

(12) Pearson, W. B. *J. Less-Common Met.* **1985**, *109*, L3-L6.

(13) Pearson, W. B. *J. Less-Common Met.* **1984**, *100*, 229-39.

(14) Nesper, R. *Angew. Chem.* **1991**, *103*, 805-834; *Angew. Chem., Int Ed*, **1991**, 30(7), 789-817.

(15) Pauling, L. *The Nature of the Chemical Bond*; Cornell University Press: New York, 1960.

(16) Pauling, L. *Die Natur der Chemischen Binding*; Verlag Chemie: Weinheim, 1976.

(17) Zintl, E.; Kaiser, H. Z *Anorg. Allg. Chem.* **1933**, *211*, 113-131.

(18) Zintl, E.; Harder, A. Z *physik. Chem.* **1931**, *154*, 47-91.

(19) Zintl, E.; Goubeau, J.; Dullenkopf, W. Z. *physik. Chem.* **1931**, *154*, 1 -46.

(20) Zintl, E.; Brauer, G. Z *physik. Chem.* **1933**, *20B*, 245-271.

(21) Zintl, E. *Angew. Chem.* **1939**, *52*, 1-6.

(22) Schäfer, H.; Eisenmann, B.; Muller, W. *Angew. Chem.* **1973**, *85*, 742.

(23) Zintl, E.; Brauer, Z. *Z. Phys. Chem.* **1933**, *B20*, 245.

(24)Hume-Rothery, W. *J. Inst. Met*. **1926**, *35*, 313.

(25) Zintl, E.; Dullenkopf, W. *Z. Phys. Chem.* **1932**, *B16*, 183.

(26) Mooser, E.; Pearson, W.B. *Prog. Semicond.* Vol. 5.

(27) Klemm, W. *Festkorperprobleme*; Vierweg: Braunschweig, 1963.

(28) Busmann, E. *Z. Anorg. Allg. Chem.* **1961**, *313*, 90.

(29) Klemm, E.; Busmann, E. *Z. Anorg. Allg. Chem.* **1963**, *319*, 297.

(30) Klemm, W.; Hohmann, E. *Alkalisilizide, Alkaligermanide, Ihre Darstellung und Einige Wichtige Eigenschaften*; interner Bericht; Unversität Münster; January 1947.

(31) Zintl, E.; Dullenkopf, W. *Z. Phys. Chem.* **1932**, *B16*, 195.

(32) Nesper, R. *Prog. Solid State Chem.* **1990**, *20*, 1.

(33) Klemm, W. *Proc. Chem. Soc.* **1959**, 329.

(34) Grimm, H.O. *Z. Elektrochem.* **1925**, *31*, 474.

(35) Grimm, H.O. *Z. Naturwiss.* **1929**, *17*, 535.

(36) Von Schnering, H.G. *Angew. Chem. Int. Ed. Engl.* **1981**, *20*, 33.

(37) Laves, F. *Naturwiss.* **1941**, *29*, 241.

(38) Matthias, B. T.; Geballe, T. H.; Compton, V. B. *Rev. Mod. Phys.* **1963**, *35*, 1-22.

(39) Matthias, B. T.; Stein, P. R. *Phys. Mod. Mater. Lect. Int. Course* **1980**, *2*,121-48.

(40) Cava, R. J. *Physica C.* **1997**, *282-287,* 27-34.

(41) Zandbergen, H. W.; Jansen, J.; Cava, R. J.; Krajewski, J. J.; Peck, W. F., Jr. *Nature* **1994**, *372*, 759-61.

(42) Cava, R. J.; Takagi, H.; Zandbergen, H. W.; Krajewski, J. J.; Peck, W. F., Jr.; Siegrist, T.; Batlogg, B.; van Dover, R. B.; Felder, R. J.; et al. *Nature* **1994**, *367,* 252-253.(43) Ku, H. C; Johnston, D. C; Matthias, B. T.; Barz, H.; Burri, G.; Rinderer, L. *Mater. Res. Bull.* **1979**, *14*, 1591-9.

(44) Roberts, B. W. *J. Phys. Chem. Ref. Data* **1976**, *5*, 581 -821.

(45) Nagamatsu, J.; Nakagawa, N.; Muranaka, T.; Zenitani, Y.; Akimitsu, J. *Nature* **2001**, *410*, 63-64.

(46) Deng, S.; Koehler, J.; Simon, A. *J. Supercond.* **2002**, *15*, 635-638.

(47) Heid, R.; Bohnen, K.-P.; Renker, B. *Adv. Solid State Phys.* **2002**, *42*, 293- 305.

(48) He, T.; Huang, Q.; Ramirez, A. P.; Wang, Y.; Regan, K. A.; Rogado, N.; Hayward, M. A.; Haas, M. K.; Slusky, J. S.; Inumara, K.; Zandbergen, H. W.; Ong, N. P.; Cava, R. J. *Nature* **2001**, *411*, 54-56.

(49) Saxena, S., Agarwal, P., Ahilan, K., Grosche, F.M., Haselwimmer, R., Steiner, M., Pugh, E., Walker, I., Julian, S., Monthoux, P., Lonzzaruch, G., Huxley, A., Sheikin, I., Braithwaite, D., Flouquet, J. *Nature* **2000,** *406*, 587

(50) Pfleiderer, C., Uhlarz, M., Hayden, S., Vollmer, R., Lohneysen, H.V., Bernhoeft, N., Lonzarich, G. *Nature* **2001**, 412, 58

(51) Aoki, D., Huxley, A., Ressouche, E., Braithwaite, D., Flouquet, J., Brison, J.-P., Lhotel, E., Paulsen, C. *Nature* **2001**, 413, 613

(52) King, R. B. *J. Solid State Chem.* **1997**, *131,* 394-398.

(53) Steglich, F.; Aarts, J.; Bredl, C. D.; Lieke, W.; Meschede, D.; Franz, W.; Schaefer, H. *Phys. Rev. Lett.* **1979**, *43,* 1892-1896.

(54) Petrovic, C; Pagliuso, P. G.; Hundley, M. F.; Movshovich, R.; Sarrao, J. L.; Thompson, J. D.; Fisk, Z.; Monthoux, P. *J. Phys.* **2001**, *13,* L337-L342.

(55) Palstra, T. T. M.; Menovsky, A. A.; Van den Berg, J.; Dirkmaat, A. J.; Kes, P. H.; Nieuwenhuys, G. J.; Mydosh, J. A. *Phys. Rev. Lett.* **1985**, *55,* 2727-2730.

(56) Meisner, G. P.; Giorgi, A. L.; Lawson, A. C; Stewart, G. R.; Willis, J. O.; Wire, M. S.; Smith, J. L. *Phys. Rev. Lett.* **1984**, *53,* 1829-1832.

(57) Stewart, G. R.; Fisk, Z.; Willis, J. O.; Smith, J. L. *Phys. Rev. Lett.* **1984**, *52,* 679-682.

(58) Kamihara, Y.; Watanabe, T.; Hirano, M.; Hosono, H. *J. Am. Chem. Soc.* **2008**, *130,* 3296-3297.

(59) Takahashi, H.; Igawa, K.; Arii, K.; Kamihara, Y.; Hirano, M.; Hosono, H. *Nature* **2008**, *453,* 376-378.

(60) Chen, X. H.; Wu, T.; Wu, G.; Liu, R. H.; Chen, H.; Fang, D. F. *Nature* **2008**, *453,*761-762.

(61) Chen, G. F.; Li, Z.; Wu, D.; Li, G.; Hu, W. Z.; Dong, J.; Zheng, P.; Luo, J. L.; Wang, N. L. *Phys. Rev. Lett.* **2008**, *100,* 247002/1-247002/4.

(62) Ren Z. A.; Che, G. C.; Dong X. L.; Yang, J. ; Lu, W.; Yi, W.; Shen X. L.; Li, Z. C.; Sun, L.L. ; Zhou F.; and Zhao, Z. X.; *Europhys. Lett.* **2008**, *83,* 17002.

(63) Bos, J. W. G. ; Penny, G. B. S. ; Rodgers, J. A. ; Sokolov, D. A. ; Huxley, A. D. ; and Attfield, J. P. *Chem. Commun.* **2008**, 3634.

(64) Lee, C. H. ; Iyo, A.; Eisaki, H. ; Kito, H. ; Fernandez-Diaz, M. T. ; Ito, T. ; Kihou, K. ; Matsuhata, H. ; Braden M. ; and Yamada, K. *J. Phys. Soc. Jpn.* **2008**, *77*, 083704.

(65) Ren, Z. A. ; Lu, W. ; Yang, J.; Yi, W.; Shen, X. L.; Li, Z. C.; Che, G. C.; Dong, X. L.; Sun, L. L.; Zhou F.; Zhao, Z. X. *Chin. Phys. Lett.* **2008**, *25*, 2215.

(66) Yang, J. ; Li, Z. C.; Lu, W.; Yi, W.; Shen, X. L.; Ren, Z. A.; Che, G. C.; Dong, X. L.; Sun, L. L.; Zhou F.; Zhao, Z. X. *Supercond. Sci. Technol.* **2008**, *21*, 082001.

(67) Ren, Z. A. ; Yang J.; Lu, W.; Yi, W.; Shen, X. L.; Li, Z. C.; Che, G. C.; Dong, X. L.; Sun, L. L.; Zhou F.; Zhao, Z. X. *Europhys. Lett.* **2008**, *82*, 57002.

(68) Chen, X. H. ; Wu, T.; Wu, G.; Liu, R. H.; Chen, H. ; Fang, D. F. *Nature*, **2008**, *453*, 761.

(69) Rozsa, S.; Schuster, H. U. Z *Naturforsch. B* **1981**, *36B,* 1668-1670.

(70) Wenz, P.; Schuster, H. U. Z. *Naturforsch. B* **1984**, *39B,* 1816-1818.

(71) Noack, M.; Schuster, H.-U. Z *Anorg. Allg. Chem.* **1994**, *620,* 1777-1780.

(72) Pfisterer, M.; Nagorsen, G. Z *Naturforsch. B* **1980**, *35B,* 703-704.

(73) Pfisterer, M.; Nagorsen, G. Z *Naturforsch. B* **1983**, *38B,* 811-814.

(74) Francois, M.; Venturini, G.; Mareche, J. F.; Malaman, B.; Roques, B. *J. Less-Common Metals* **1985,** *113,* 231-237'.

(75) Jeitschko, W.; Glaum, R.; Boonk, L. *J. Solid State Chem.* **1987,** *69,* 93-100.

(76) Jeitschko, W.; Glaum, R.; Boonk, L. *J. Solid State Chem.* **1987,** *69,* 93-100.

(77) Mine, T.; Yanagi, H.; Kamiya, T.; Kamihara, Y.; Hirano, M.; Hosono, H. *Solid State Commun.* **2008,** *147,* 111-113.

(78) Cava, R. J.; Takagi, H.; Batlogg, B.; Zandbergen, H. W.; Krajewski, J. J.; Peck, W. F., Jr.; van Dover, R. B.; Felder, R. J.; Siegrist, T.; et al. *Nature* **1994,** *367,* 146-148.

Chapter 2

Synthesis and Characterization

2.1 Synthesis

The objective of this study is to synthesize and characterize the layered CoGe and CoAs based compounds and to investigate their superconducting properties. In solid state chemistry, the success of the research can be improved through clever choices of starting materials, as well as with the appropriate temperature and pressure settings during the synthesis. Because of the difficulty in the purification of the product, it is quite necessary to take every possible precaution to prevent unwanted impurities going into the system.[1]

One of the oldest methods of solid state synthesis is the ceramic method or sintering. To obtain a state of equilibrium, high temperature is required because of low diffusion rates and the large diffusion distances associated with solid state reactions that generally yield crystalline and thermodynamically stable solids.[2] The conditions for a successful synthesis can be obtained from the known or estimated phase diagrams.

Nevertheless, it is difficult to obtain the homogenous sample owing to its slow diffusion rate and large diffusion path length in solid state reaction.[3] To minimize this, it is necessary to melt or lower the particle size of the reactants. For this purpose, generally, the mixture is taken out, reground to bring the fresh surface in contact, press into pellet in a hydraulic press, and sinter in a furnace for prolonged periods. And this pressed pellet when heated at an elevated temperature below its melting point, powder particles fuse together decreasing the voids and increasing the density of the powders.

2.1.1 Materials

All reagents and products were stored and handled in a purified Ar atmosphere glove box (Figure 2.1), and manipulated on a vacuum line equipped with a mercury diffusion pump. The glove boxes used were continuously purged with dry argon, and the atmosphere cleaned by molecular sieves and oxygen scavengers. The moisture content of the dry box atmosphere was monitored on a regular basis and maintained at less than 1 ppm. These levels were also tested by using 60 watt light bulbs. Based on the life of the light bulb, the amount of oxygen in the glove box was calculated. Periodic regeneration of the catalyst was carried out for ensuring the inert atmosphere inside the glove box. The regeneration gas used was 5% hydrogen and 95% nitrogen gas mixture from Matheson Trigas.

In this work, all high-purity metals were obtained from commercial sources. The sources and forms of all reagents are presented in Table 2.1.1. Most of them were used as received. Whenever appropriate, the surfaces of the various solid reactants were scraped and cleaned before use. The niobium tubes and tantalum tubes were washed with the 55% H_2SO_4, 25% HNO_3 and 20% HF. The alkali metal K was received as 5 and 25g samples in glass ampoules under vacuum from Alfa Aesar. The alkaline earth metals obtained from Aldrich were dendritic pieced ampouled under argon.

2.1.2 Containers

The solid state syntheses were carried out at high temperature. The containers niobium and tantalum tubes were used due to the corrosive nature of alkali and alkaline earth metals. Seamless niobium and tantalum tubes were chosen as inert reaction containers in this work. Except for germanium, none of the electropositive metals used in

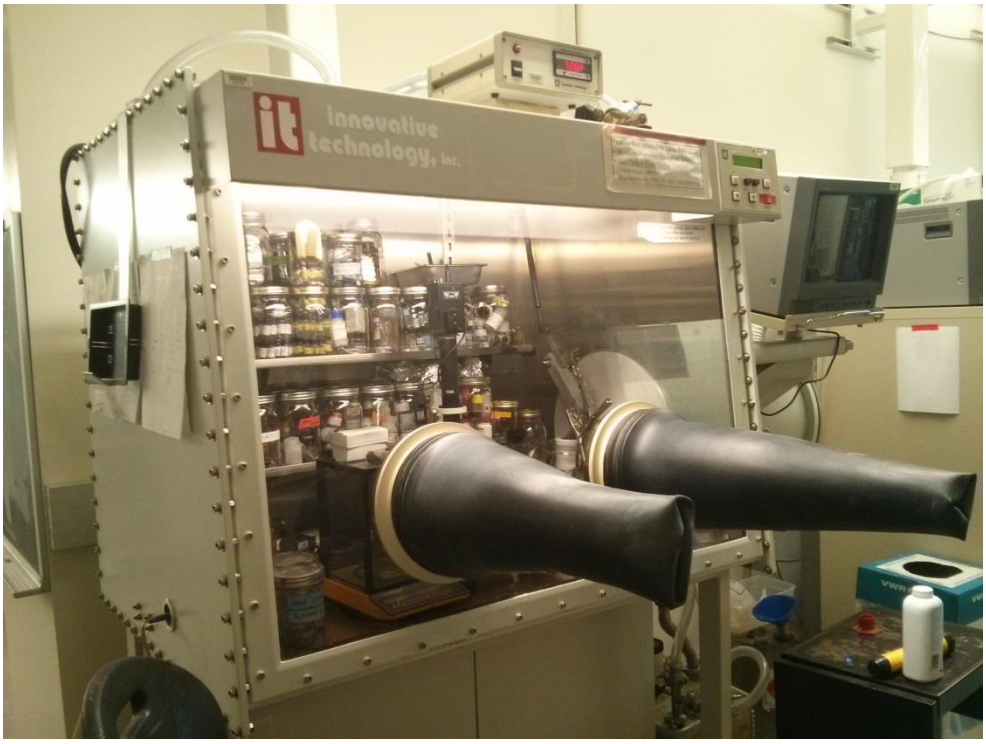

Figure 2.1: Glovebox (argon atmpsphere)

Material	Form	Purity	Source	Melting Pt.(^{o}C)
K	Paste	99.95%	Alfa Aesar	63.4
Ca	Pieces	99.99%	Aldrich	839
Sr	Pieces	99.9%	Aldrich	768
Ba	Dendrites	99.99%	Aldrich	729
Co	Ingot	99.99%		1495
Co	Powder	99.99%	Alfa Aesar	1495
As	Lumps	99.99%	Alfa Aesar	Sublime
Ge	Chip	99.99%	Aldrich	937

Table 2.1: Materials used during synthesis

this study is known to form binary compounds with niobium or tantalum or exhibit any significant solubility. Niobium forms a variety of binary alloys with group 13 and 14 elements (Nb_3Ge, Nb_5Ge_3 etc.). However, the reactivity's of the elements of group 13 and 14 towards the tube materials is much lower than with the alkali, alkali-earth and rare earth metals.

Because of the sublime nature of arsenic, use of an appropriate reaction crucible is required for carrying out the reactions of highly reducing alkali and alkaline earth metals. Due to the limited contact and poor diffusion between reactants, SiO_2, fused silica ('quartz') is widely used as a container. In the synthesis of binary precursors, FeAs, CoAs, MnAs and other transition metal arsenides fused silica was used as container. However, the reaction of SiO_2 with H_2:

$SiO_2(s) + H_2 \longrightarrow SiO + H_2O$

at high temperatures (~1000°C) results in the effective transport of Si and O from the wall of quartz to the reactants. The H_2 transporting agent may arise from the degassing of the reactant metals or, more frequently, from the reduction of traces of water that are evolved from silica upon heating. In addition, contamination from fingerprints can lead to the transport of silica to the reactants. Thus, proper cleaning and drying of the quartz containers prior to use is necessary in all synthesis performed in this study. Inert metal containers were also used due to the corrosive nature of pure alkali and alkaline-earth metals. Among the traditional refractory materials - Nb, Ta, Mo, and W, the first two are the most versatile in terms of ductility, strength, and ease of fabrication and welding. [4] On the other hand, direct synthesis of metal pnictides in seamless Nb or Ta containers may result in a variety of binary compounds of the metal containers ($AsNb_3$, As_2Nb, Nb_5Ge_3

etc.).[5,6] Therefore, using the binary precursors CoAs with alkali and alkaline earth metals will help minimize the formation of binary impurities.

Before loading the reacting samples, all Nb and Ta tubes were cleaned using a solution made from concentrated H_2SO_4, concentrated HNO_3 and 48% HF in the proportion of 55:25:20 by volume. The clean Nb tubes were immersed in the acid solution, rinsed several times with distilled water, and dried in an oven. Then after, it is crimped on one end and sealed by arc welding under an inert argon atmosphere. The reactants were then loaded into the Nb/Ta tubes and welded. All manipulations were carried out within an argon atmosphere inside the glovebox. Reaction vessels were taken out of the glove box and quickly transferred to the arc welded and sealed using the argon atmosphere. The sealed reaction tubes were then placed in silica jackets which are then evacuated under vacuum and sealed under vacuum to prevent the oxidization from moist air.

2.1.3 Furnaces

A temperature of 1100^{o}C was usually high enough to melt the alkali, alkaline-earth compounds in this work. Most of the high-temperature reactions were performed using regular high-temperature resistance furnaces, which were controlled by programmable temperature controller.

Induction furnaces were used for synthesis at high temperatures (temperature between 1000°C and 1700°C). The induction furnace, which is from Ameritherm Inc., uses water-cooled AC power supply to provide electricity with low voltage. Here very high current and high frequency, this energy is delivered over the RF power cable to the

water-cooled Heat Station and this creates a magnetic field around the work-piece, heating it with precise control of the temperature and timing.

Arc-melting furnaces were also used for the precursor synthesis at high temperatures (T > 2000 °C). The arc-melting furnace, from Centorr/Vacuum Industries model 5SA Single Arc Furnace, is equipped with a Maxstar 91 CC-DC inverter welding power source. Pre-weighed samples within a tightly closed glass container were transferred quickly from glove box to the arc-melting furnace. Once the furnace was sealed, it was evacuated then flushed with argon several times. The samples were then melted under continuously flowing of argon on a clean water-cooled copper hearth. Small pieces of Ti metal were used as "getters" of oxygen and moisture.

2.1.4 Synthetic Method

The heat treatment was performed in steps. The reactions were heated at a rate of 1^{o}C/min to a certain temperature, held at that temperature for 2-4 days and slowly cooled at 1^{o}C/min to room temperature. The reaction temperature and reaction time for different synthesis were different.

2.2 Characterization Methods and Techniques

2.2.1 Powder X-ray diffraction

All bulk samples were analyzed using powder X-ray diffraction for phase identification and phase purity determination. The samples were ground into fine powder and placed on-zero background flat sample holders. The air-sensitive samples were prepared within the glove box and then covered with Kapton film. The Kapton film was used to protect the sample from the air and this caused a small bump between 10 and 15 degrees on powder pattern. Powder diffraction data were collected on a Panalytical X'pert

Diffractometer with 9-9 geometry and monochromatic Cu Ka 0.02°/sec from 2theta = 5° to 100°. Phase identification from the powder pattern was performed by matching peaks with those of known compounds from database and calculated patterns from single crystal data. WinXPow was used to generate calculated powder pattern based on single crystal data. Cell parameters were indexed by JANA 2006. Powder refinements were done for these compounds: $CaCo_2Ge_2$, $SrCo_2Ge_2$, $BaCo_2As_2$, KCo_2As_2 and $Ba_xK_{1-x}Co_2As_2$.

2.2.2 Single Crystal X-Ray Diffraction

Single crystal X-ray analysis was done using a fully integrated high-resolution, Rigaku R-AXIS RAPID II diffractometer equipped with large-area curved imaging plate (IP) detectors. The selected single crystals were covered with a layer of Paratone-N oil to protect them from air and moisture and placed at the tip of glass fibers. For very sensitive samples, the crystals were placed in 0.3 mm diameter glass capillaries. Monochromatic Mo $K\alpha_1$ radiation (λ=0.71073Å) was used to collect a full hemisphere of data with the narrow-frame method. The data were integrated using the Rigaku CrystalClear program, and the intensities corrected for Lorentz factor, polarization, air absorption, and absorption due to variation in the path length. Multi-scan absorption correction was applied and redundant reflections were averaged. Final cell parameters were refined using reflections having I>10 σ(I). The structure was solved by direct methods refined by full-matrix least-squares calculations on F^2, the thermal motion of all atoms were treated anisotropically. All calculations were made with using the SHELXS-97[7] and SHELXL-97. [8]

2.2.3 Physical Property Measurements

Magnetic Property Measurements: The temperature dependence of the dc magnetic susceptibility measurements were performed with Superconducting Quantum Interference Devices (SQUID) Magnetometers in Dr. Lorenz's lab (Quantum Design MPMS-XL) with fields up to 5T. The measurements of ACo_2As_2(A=K), $AeCo_2As_2$(Ae= Ba), AxAe1-xCo2As2 (with doping samples of K into Ba sites) were performed by Dr. Bernd Lorenz and Dr. Melissa Gooch.

The SQUID is a very sensitive magnetometer which is used to measure extremely small magnetic fields by using superconducting loops containing Josephson junctions. Data collection temperature normally is from 300 K to 1.8K. Because magnetic and thermal history play the role on the magnetic properties of the sample, magnetic measurements were performed under different conditions, which are described below:

Zero field-cooled (ZFC) Measurements

The material is cooled in the zero-magnetic fields from a temperature above the studied phase transition temperature to a desired temperature. Then, a magnetic field is applied and the magnetization is measured as a function of increasing temperature during the warming process.

Field-cooled Measurements

The sample is cooled with a constant magnetic field from a temperature above Tc. The magnetization is measured during the cooling and warming process.

Hysteresis Loop Measurements

The sample is cooled to a desired temperature without applying any magnetic

field, and then the field is swept while measuring the magnetization. For a given material, the magnetic susceptibility can vary based upon two factors, temperature (T) and applied magnetic field (Ho). The behavior of the material as the temperature and/or field is changed gives rise to four different types of classifications: paramagnetism, diamagnetism, ferromagnetism, and antiferromagnetism. The field and temperature dependencies of these magnetic classes are described in Table 2.2 below. A superconducting material, cooled below its critical temperature in the presence of an applied magnetic field, expels all magnetic flux from its interior. If a magnetic field is applied after the substance has been cooled below its critical temperature, the magnetic flux is excluded from the superconductor. The Meissner effect shows that the superconductor is a perfect diamagnet. For superconductors, the magnetic moment vs. temperature data was plotted using volume magnetic susceptibility χ vs. temperature.

$$\chi = \frac{M}{H} = \frac{m}{Volume \times H} = \frac{m \times \rho}{H \times W}$$

where m = magnetic moment (emu), M=Magnetization (magnetic moment per unit volume, emu/cm^3), p = density (g/ cm^3), W = sample mass (g), H = applied field (Oe).

The volume fraction gives an indication on whether the superconductivity is bulk or not.

2.2.4 Electrical Conductivities Measurements

The electrical resistivity, p, of the samples were measured as a function of temperature p (T) employing a standard 4-probe method using a Linear Research LR-700 ac bridge operated at 19 Hz in Dr. Berd Lorenz's lab. The measurements of $CaCo_2Ge_2$, $BaCo_2As_2$and KCo_2As_2 compounds were performed by Dr. Bernd Lorenz. The wire configuration for measurement is as shown in Figure 2.2.

	Sign of χ	Dependence on H_o	Origin of Effect
Diamagnetism	-	Independent	Field induced circulation of electron pairs
Paramagnetism	+	Dependent	Angular momentum of the electron
Ferromagnetism	+	Dependent	Parallel alignment of unpaired electron pairs
Antiferromagnetism	+	Dependent	Antiparallel alignment of unpaired electron spins

Table 2.2: Typical Magnetic Behavior of Solids.

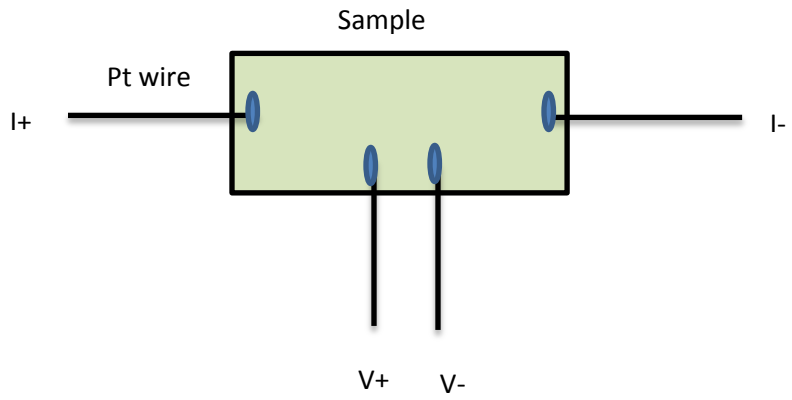

Figure 2.2: Configuration for the resistance measurement. V+ means positive lead voltage and V- means negative voltage lead. I+ denotes positive current lead and I- denotes negative current lead.

R**eferences**

(1) Schmalzreid, H. *Solid State Reactions,* 1971.

(2) Schaefer, H. *Angew. Chem. Int. Ed* **1971**, *10,* 43-50.

(3) Smart, L. E.; Moore, E. A. *Solid State Chemistry: An Introduction Third Edition;* CRC Press, 2005.

(4) Corbett, J. D. *Inorganic Syntheses* **1983**, *22,* 15-22.

(5) Jorda, J. L.; Fluekiger, R.; Mueller, J. *J. Less-Common Metals* **1978**, *62,* 25-37.

(6) Hector, A. L.; Parkin, I. P. *Z. Naturforsch. B* **1994**, *49,* 477-82.

(7). Sheldrick, G.M; SCHELXS-97, *Program for the Determination of Crystal Structures University of Goettingen* (Germany) 1997.

(8) Sheldrick, G.M.; SCHELXL-97, *Program for Crystal Structure Refinement University of Goettingen* (Germany) 1997.

Chapter 3

$CaCo_2Ge_2$ and $SrCo_2Ge_2$ compounds

3.1 Introduction

Generally, for the superconductivity to occur, the parent 122 compounds that crystallize with the $ThCr_2Si_2$ structure need some kind of substitution at one of the atom sites. The substitution may lead to electron-poor,[1] electron-rich[2] or isoelectronic substitution.[3] Due to the large variety of compounds that crystallize with $ThCr_2Si_2$ structure they have high chemical flexibility and a number of substitutions possibilities are given. In this regard we try to synthesize the 122 $AeCo_2Ge_2$ (where Ae=Ca, Sr and Ba) and investigate their physical properties that might give us some idea on doping with whether with electrons or holes.

3.2 Experimental Sections

Reagents: The following reagents were used as received and were stored and handled under argon atmosphere in glovebox: Ba (dendrites, 99.99% Aldrich), Sr (pieces, 99.9% Aldrich), Ba (dendrites, Alfa Aesar), Ca (pieces, 99.99% Aldrich), Co ingot, Ge chip (99.99%) Aldrich.

Synthesis: Stoichiometric amounts of cobalt and germanium pieces were taken in the copper hearth and placed in an arc-melting furnace. The chamber of the arc melting furnace was evacuated followed by purging with argon. The process was repeated three times to get rid of any oxygen and moisture. Then, it was arc-melted using titanium buttons as an oxygen "getter". The metal pieces were arc-melted under flowing pure argon gas for about 30 seconds (with the current of 20 A). The arc melted cobalt

germanium button was flipped over and arc melted three times to ensure homogeneity. The loss by mass was less than 1%. It was then taken into the glovebox where it was loaded in the tantalum tube along with calcium or strontium or barium. The tube was welded and kept in the evacuated quartz jacket and heated in the induction furnace at 40% voltage, i.e., at 1300^{o}C for 2hrs. The reaction was quenched in air. X-ray powder pure phase of $CaCo_2Ge_2$ and $SrCo_2Ge_2$ were able to be obtained after investigating by powder X-ray diffraction (Panalytical X'pert diffractometer). The tantalum tubes and quartz tubes were washed and dried in the oven prior to use. All the preparative manipulations were carried out in the purified argon filled glove box with total O_2 and H_2O level less than 1 ppm. However, the synthesis of $BaCo_2Ge_2$ was unsuccessful.

3.3 Crystallography of $CaCo_2Ge_2$ and $SrCo_2Ge_2$

The single crystal data have been reported in 1976[4] and 1996[5]. High-purity phases of the $CaCo_2Ge_2$ and $SrCo_2Ge_2$ were able to be synthesized. The crystals obtained from the reaction were studied by powder diffractometer (Panalytical X-pert diffractometer) as well as single crystal diffractometer (Rigaku R-AXIS RAPID II diffractometer). The powder patterns were indexed and the refined lattice constants were similar to those obtained by single crystal diffraction. The structure was solved by direct methods refined by full-matrix least-squares calculations on F^2, the thermal motion of all atoms were treated anisotropically. The crystal refinement data is shown in the table 3.1. Final least-square refinements resulted in refinement parameter of $R_f = 0.0419$ and $R_w = 0.0552$. The compounds $CaCo_2Ge_2$ and $SrCo_2Ge_2$ adopt the $ThCr_2Si_2$ structure type. This Structure type consists of $[Co_2Ge_2]^{2-}$ layers between which the A^{2+} cations are situated.

Empirical Formula	$CaCo_2Ge_2$	$SrCo_2Ge_2$
Formula weight	303.12	350.66
Crystal System	Tetragonal	Tetragonal
Space group	*I4/mmm*	*I4/mmm*
Unit cell	a = 3.99580(10) Å c = 10.3086(7) Å α=ϐ=ϒ=90°	a = 4.0752(3) Å c = 10.6809(8) Å α=ϐ=ϒ=90°
Volume	164.59(1) $Å^3$	177.38(2) $Å^3$
Z	2	2
Density	6.116g/cm^3	6.565g/cm^3
Crystal Size	0.04×0.04×0.02 mm^3	0.02×0.02×0.06 mm^3
Theta range	5.47 to 62.58°	5.36 to 42.08°
Reflections collected	5604	1024
Refinement method	Full-matrix least-squares on F2	Full-matrix least-squares on F2
Data/ restraints/parameters	412/0/9	218/0/9
Goodness of fit on F2	1.339	1.446
Final R indices	R_1=0.0419, wR_2=0.0052	R_1=0.00192, wR_2=0.0444
R indices (all data)	R_1=0.0547, $wR_{2=.}$0581	R_1=0.0199, wR_2=0.0446

Table 3.1: Crystal data and structure refinement.

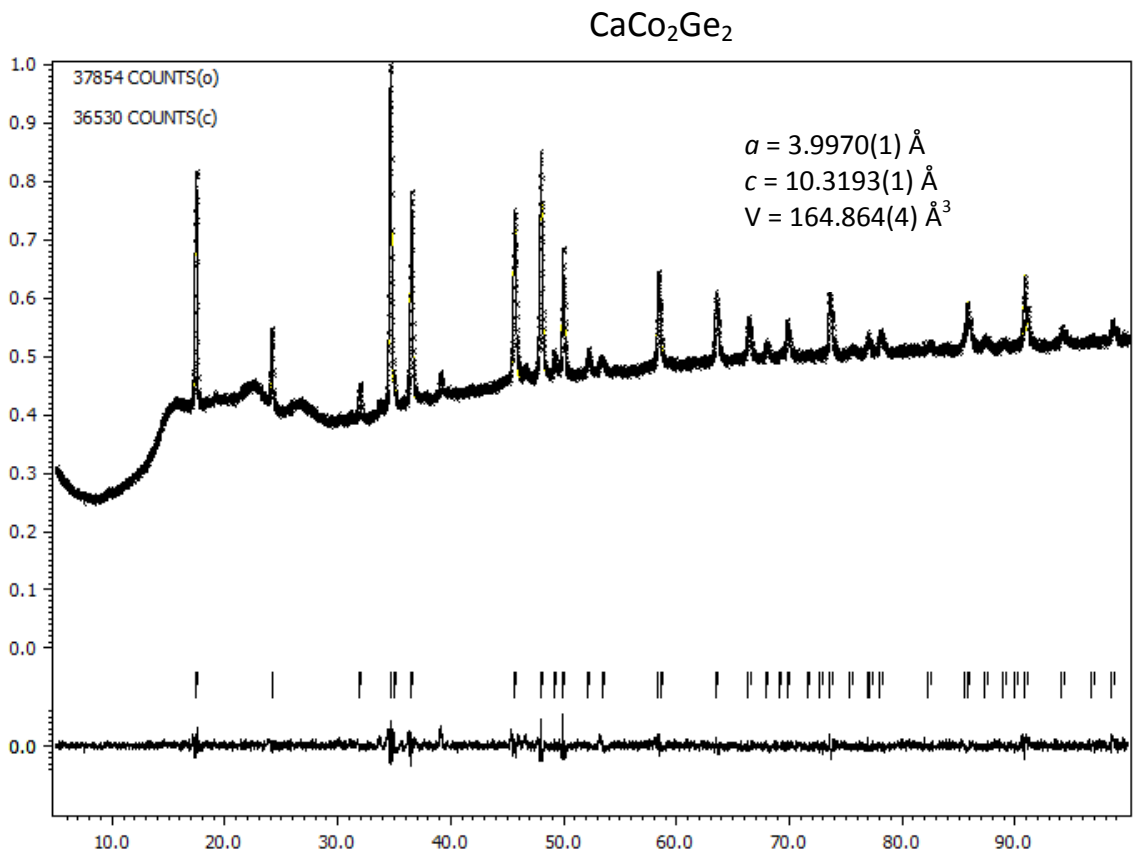

Figure 3.1: Powder diffraction pattern of $CaCo_2Ge_2$ obtained from the le Bail profile refinement. The middle one depicts the location of peaks whereas the one at the bottom shows the difference between the calculated and observed peaks.

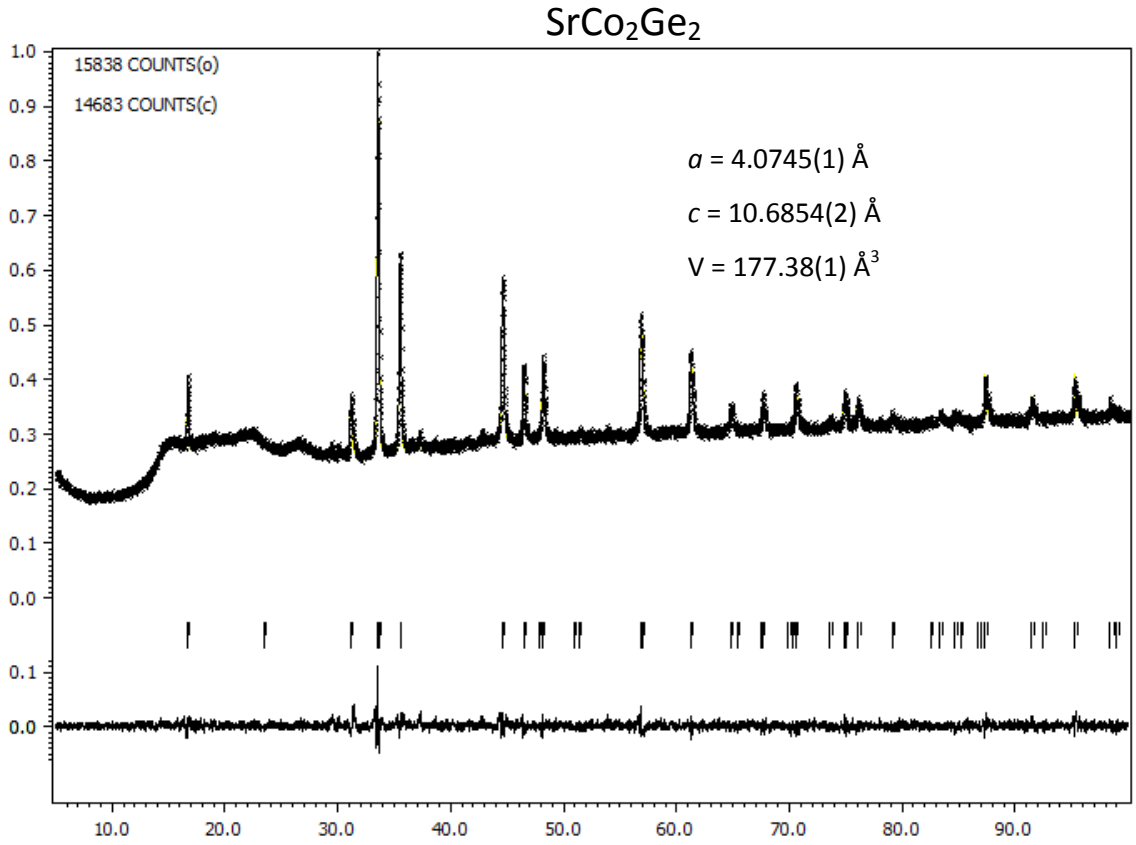

Figure 3.2: Powder diffraction pattern of $SrCo_2Ge_2$ obtained from the le Bail profile refinement. The middle one depicts the location of peaks whereas the one at the bottom shows the difference between the calculated and observed peaks.

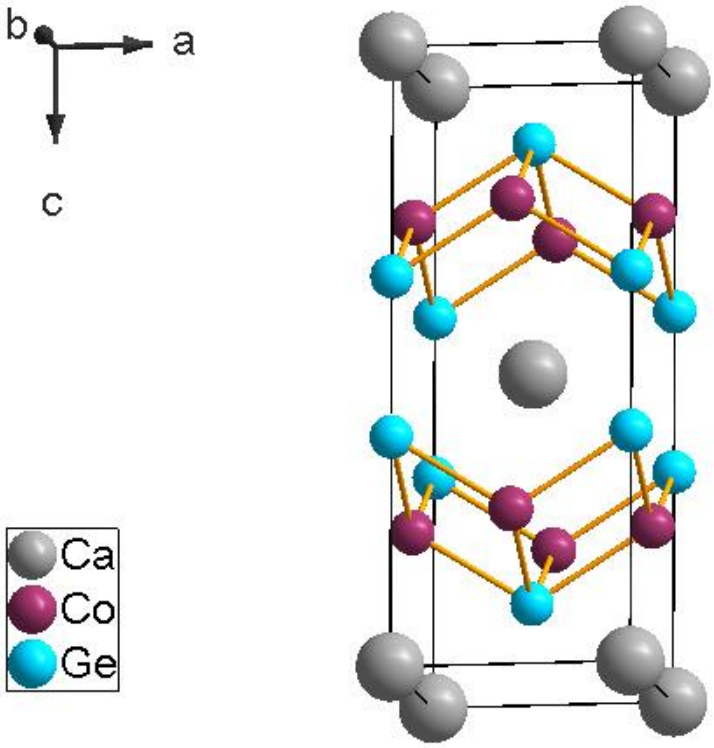

Figure 3.3: Unit cell of $CaCo_2Ge_2$ viewed along b. Co and Ge atoms form the layered network between which Ca atoms are placed.

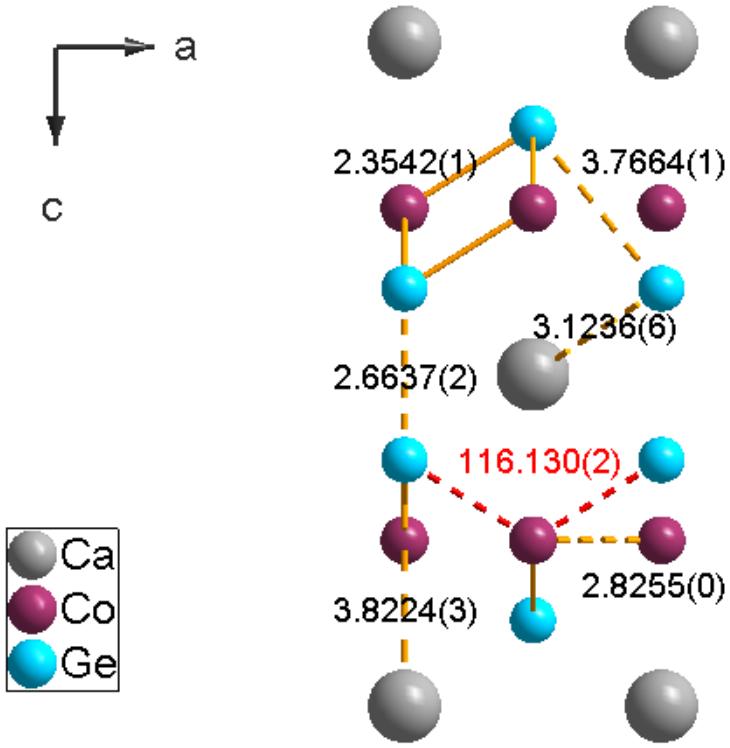

Figure 3.4: Arrangement of atoms showing bond distance (Å) and bond angles(^{o}) in $CaCo_2Ge_2$. Ca is surrounded by eight Ge atoms. Each Ge is coordinated to eight Ca atoms. And Co is coordinated to four Ge atoms.

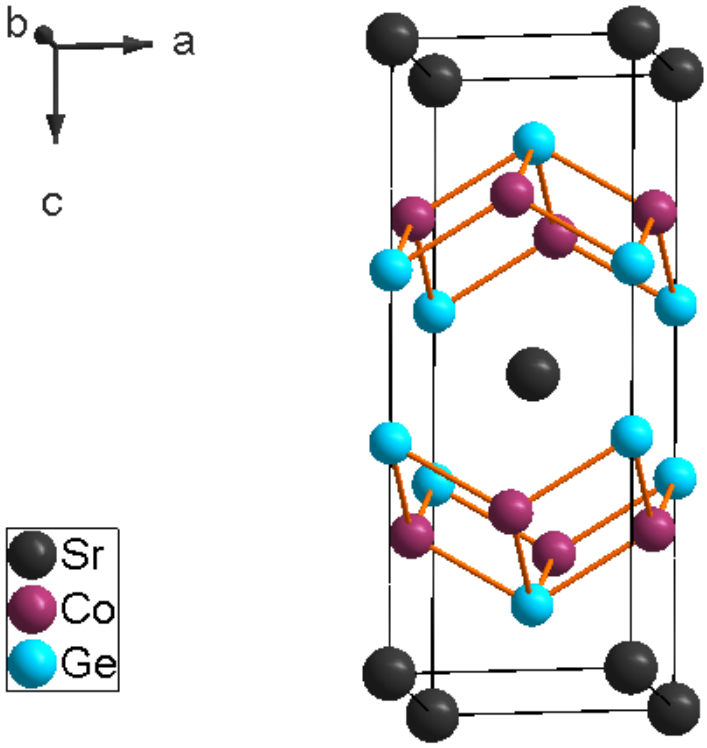

Figure 3.5: Unit cell of $SrCo_2Ge_2$ viewed along b axes. Co and Ge form the network between which Sr atoms are situated.

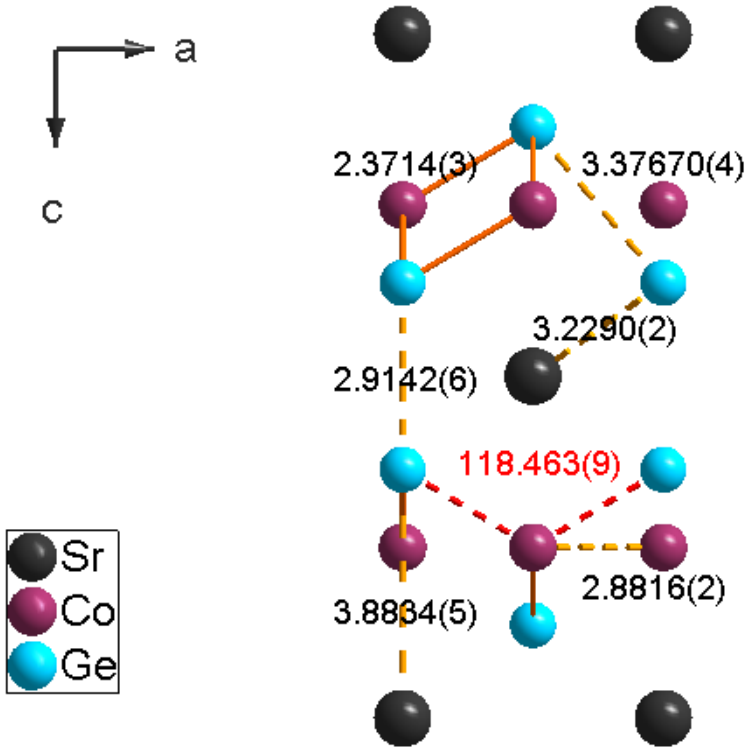

Figure 3.6: Arrangement of atoms in $SrCo_2Ge_2$ showing bond distance (Å) and bond angles (^{o}). Each Sr atom is surrounded by eight germanium atoms.

(a)

Compound	*a*/Å	*c*/ Å	V/Å^3	*c*/*a*	Co-Ge/Å	Ge-Ge/Å	Ge-Co-Ge/^{o}
$CaCo_2Ge_2$	3.9958(1)	10.3086(7)	164.59(13)	2.579	2.3542(1)	2.6637(2)	116.130(2)
$SrCo_2Ge_2$	4.0752(3)	10.6809(8)	177.38(2)	2.621	2.3714(3)	2.9142(6)	118.463(9)

(b)

Compound	*a*/Å	*c*/ Å	V/Å^3	*c*/*a*	Co-Ge/Å	Ge-Ge/Å	Ge-Co-Ge/^{o}	Ref
$CaCo_2Ge_2$	3.99	10.30	163.94	2.58	2.35	2.67	116.24	[4]
$SrCo_2Ge_2$	4.08	10.65	177.28	2.61	2.37	2.90	118.48	[5]

Table 3.2: Main interatomic distances in $CaCo_2Ge_2$ and $SrCo_2Ge_2$ compounds from **(a)** single crystal refinement and **(b)** from published reports.

These layers can be described as being built of $CoGe_4$ tetrahedra, with strong covalent Co-Ge interactions and weaker Ge-Ge interactions.

In Table 3.2, the crystallographic data, including the unit cell, the Co-Ge and the Ge-Ge distances as well as the Ge-Co-Ge angle are presented. These data are in good agreement with the published report which is tabulated in the Table 3.2b. Thus, I concluded that the interlayer Ge-Ge distances increases if calcium is substituted by the larger strontium. And this is a consequence of the size effects. The Ge-Ge bonding between the neighboring Co_2Ge_2 layers pulls the layers close together with a *c*/*a* ratio of 2.579 and 2.621 for $CaCo_2Ge_2$ and $SrCo_2Ge_2$ respectively. Choosing the ionic size in Ionic Radii in Crystal' from the Acta Cryst. (1976). A32, 751 by R. D. Shannon one can see that lattice parameter *a*, *c*, *c/a* ratio, and volume of this type of compounds increase almost linearly with the increase of the ionic size of alkali or alkaline earth atoms. This character indicates that Co_2Ge_2 layers are "expanding" as we increase the interlayer size of the alkali or alkaline earth element, resulting in longer Ge-Ge distance. We also observe a slight increase in Co-Ge distance. The Ge-Co-Ge angle also increases from 116^o to 118^o as strontium substitute the calcium atoms. So, I concluded that the substitution with the larger cations, in this case, calcium being substituted by strontium, enforces not only the elongation of the unit cell and the enlargement of the Ge-Ge distance but also the flattening of the $CoGe_4$ tetrahedron. From the table, it can also be observed that the vertical angle Ge-Co-Ge is increased with the substitution of calcium by strontium atoms.

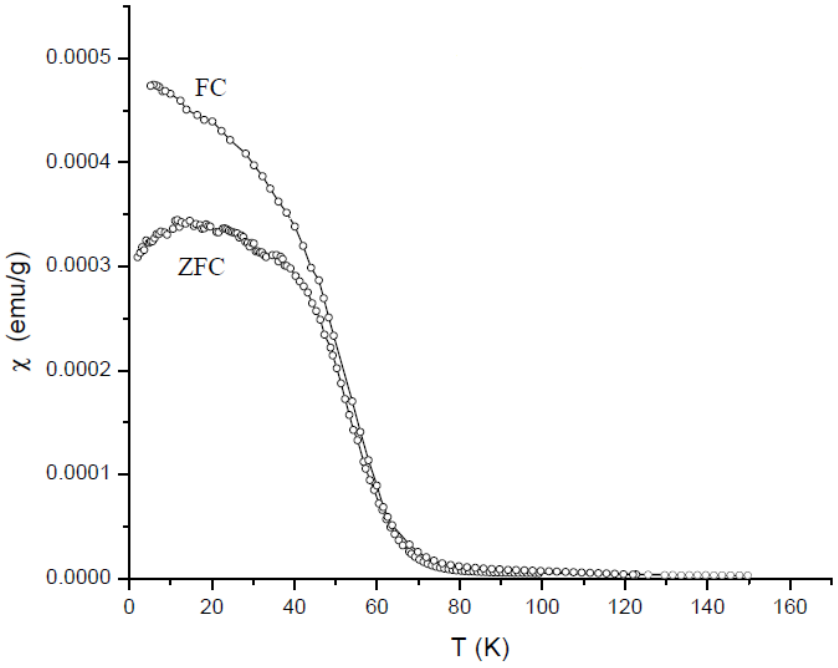

Figure 3.7: Magnetic Susceptibility as a function of temperature for $CaCo_2Ge_2$.

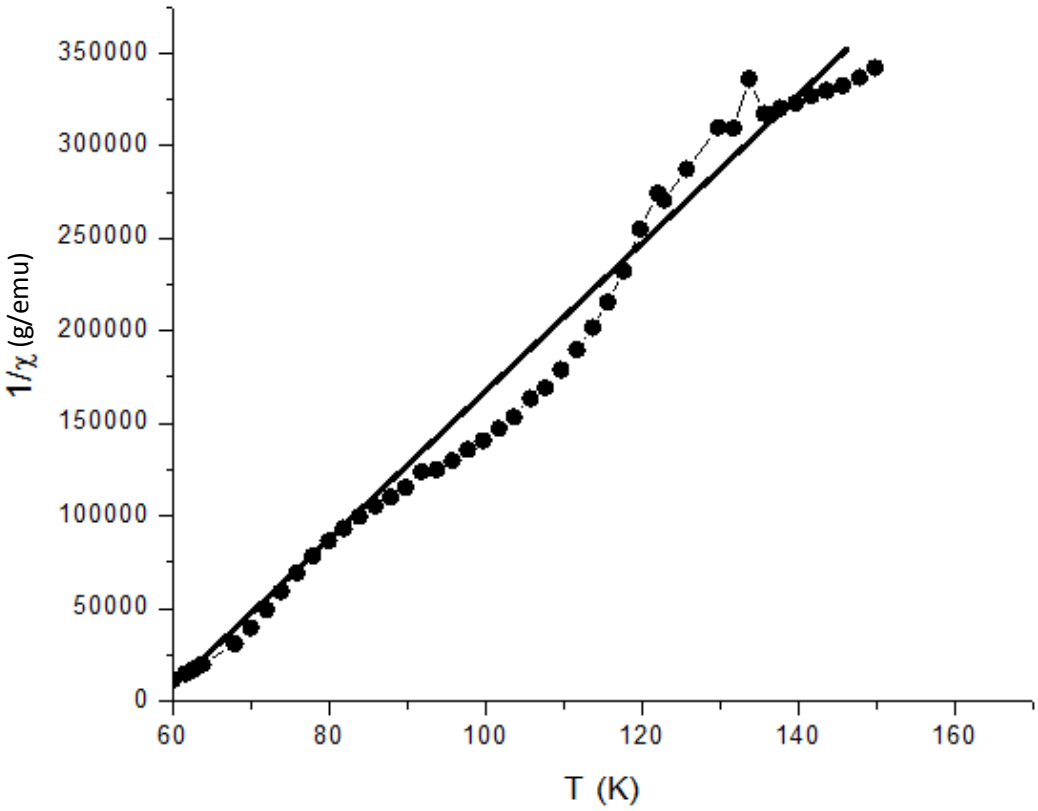

Figure 3.8: $1/\chi$ vs T plot for the compound $CaCo_2Ge_2$. A straight line is drawn. And it cannot fit into the plot. Thus, the compound does not follow Curie-Weiss law.

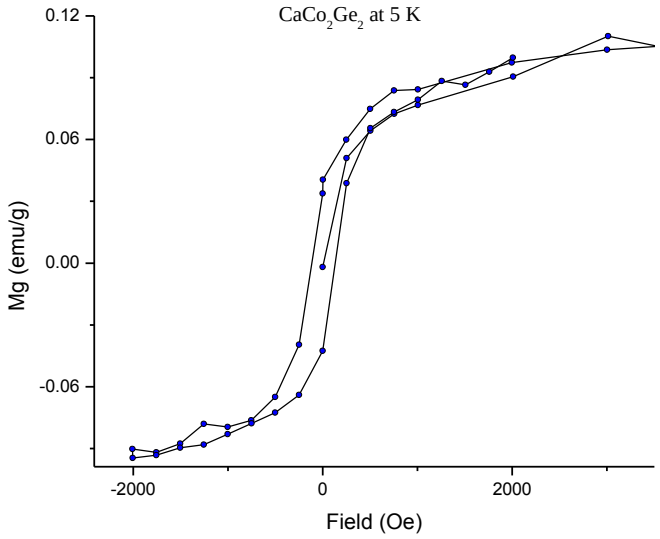

Figure 3.9: Magnetization of $CaCo_2Ge_2$ at 5K measured as a function of magnetic field. It shows the presence of small hysteresis at about 120 Oe.

.

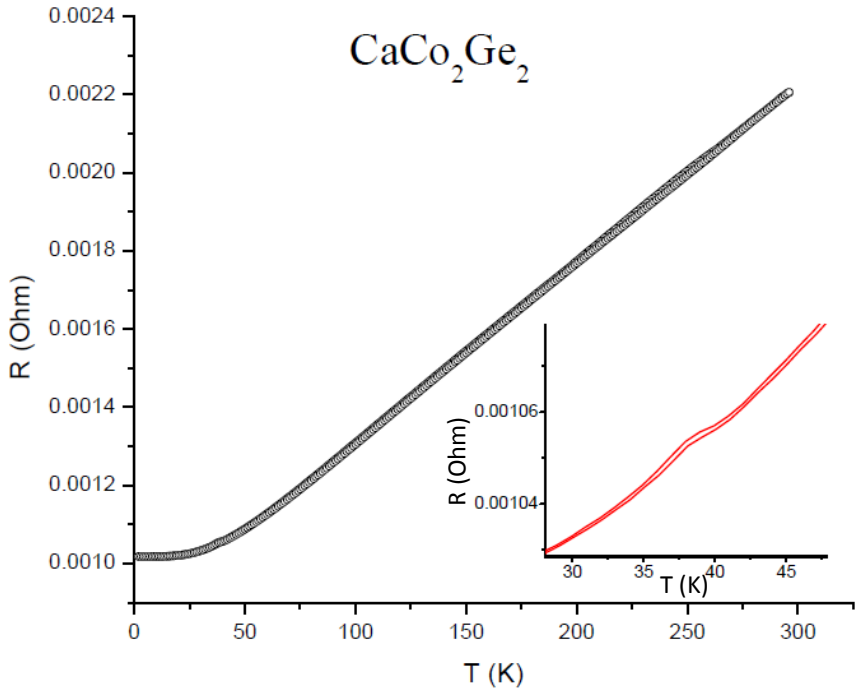

Figure 3.10: Resistance vs temperature for $CaCo_2Ge_2$ measured between 0 and 300K. The inset shows the measurement of resistance between 30 and 45 ohms. From this, the hump at 38K is confirmed.

3.3Properties of $CaCo_2Ge_2$

3.3.1 Magnetic Susceptibility Measurements

The magnetic properties were performed on Quantum Design SQUID Magnetometer with the field up to 5T. The samples were loaded in gel capsule, sealed in the messenger during transfer, and then quickly moved into SQUID. Zero field-cooled (ZFC) and field cooled (FC) measurements were performed.

Figure 3.7 shows the magnetic susceptibility as a function of temperature. Below 50 K, there is large increase of magnetic moment and the graph splits in zero field cool and field cool. This magnetic transition might be due to either ferromagnetic (FM) transition.

Figure 3.8 depicts the plot of $1/\chi$ versus temperature. Curie-Weiss law for magnetic materials is given by the equation:

$$\frac{1}{\chi} = \frac{T}{c} \pm \frac{\Theta}{c}$$

where c=curie constant; Θ= critical temperature; χ= magnetic susceptibility and T= temperature; + sign is for ferromagnetic and – sign is for the antiferromagnetic.

If $\frac{1}{\chi}$ is plotted against T, it should be a straight line. However, from the data, we did not get a straight line. Therefore, the compound $CaCo_2Ge_2$ does not follow Curie-Weiss law.

Figure 3.9 shows the presence of small hysteresis of ~ 120 Oe at 5 K and saturation of its value at higher fields confirms that the magnetic transition seen at 50 K is due to weak FM transition.

3.3.2 Resistivity Measurement for $CaCo_2Ge_2$

The resistance measurements were done using Linear Resistance Bridge (LR-700) in Dr. Lorenz's lab. Figure 3.10 shows the resistance as a function of temperature. The resistance decreases with a decrease in temperature and however there is finite resistance at low temperature which might be due to scattering electrons with lattice. A slight hump seen at 40 K might be due to weak ferromagnetic transition seen in magnetic measurement. Thus $CaCo_2Ge_2$ is a metal with weak ferromagnetic behavior at low temperature.

Conclusion

The compounds $CaCo_2Ge_2$ and $SrCo_2Ge_2$ were successfully prepared through solid state synthesis. The magnetic measurements and resitance measurement data reveal $CaCo_2Ge_2$ to be a metal with weakly ferromagnet. As the title compounds are isoelectronic to $AeFe_2As_2$ (Ae=Ca, Sr, Ba) further experiments concerning the doping with alkali metals as well as with lanthanum can be done. The substitution of Ge with the As leads to an increase in an electron.

References

(1) Rotter M.; Tegel M.; Johrendt D. *Phys. Rev. Lett.* **2008,** *101*, 107006.

(2) Leithe-Jasper A.; Schnelle W.; Geibel C.; Rosner H. *Phys. Rev. Lett.* **2008,** *101*, 207004.

(3) Tao Q.; Jiang S.; Feng C.; Wang C.; Dai J.; Cao G.; Xu Z. *Phys. Rev. Lett.* **2009**, *102*, 137002.

(4) Dorrshceidt W.; Niess N, Schaffer H. *Z. Naturforsch.* **1976**, *31b*, 890-891

(5) Venturini G.; Malaman B. *J. Alloys Compds.* **1996**, *235*, 201

Chapter 4

ACo_2As_2 and $AeCo_2As_2$ Compounds with $ThCr_2Si_2$ Structure Type

4.1 Introduction

As we substitute Co for Fe in 122 intermetallics, an increase in electron count is observed. The T_2As_2 in the AT_2As_2 (A=K) and $AeCo_2As_2$ (Ae=Ba) compounds draw a lot of attention particularly because doping Fe with Co in the $BaFe_2As_2$ has induced superconductivity. The Co_2As_2 layers in these compounds are separated with alkali or alkaline earth metal layers. What different properties will these compounds have compared to Fe_2As_2 compounds? As we know, in the large family of $ThCr_2Si_2$ type compounds, superconductivity was observed at temperatures below 5K, as in $LaIr_2Ge_2$,[1,2] $LaRu_2P_2$,[3] $BaNi_2P_2$,[4] even though closely-related rare earth borocarbides are known for Tc's up to 26K in YPd_2B_2C[5]. Does superconducting occur in these compounds? Or on the various doped samples in these systems? With this in mind, we try to synthesize and investigate the properties of these alkali and alkaline earth ACo_2As_2 and $AeCo_2As_2$ system. Here, the synthesis, structure and physical properties of these compounds are reported.

4.2 Experimental Sections

Reagents: The following reagents were used as received and were stored and handled within an argon atmosphere glovebox: K (99.95% metal basis, Alfa), Co (powder, 99.98% Alfa Aesar), Ba (dendrites, 99.99% Aldrich), As (lumps, 99.99% Alfa Aesar).

Synthesis: The quartz tubes and niobium tubes were cleaned and dried in the oven to avoid the moisture residue inside and then brought into the glovebox. As lumps was ground. The powdered As was mixed stoichiomerically with Co powder and ground together. The powdered Co-As in the stoichiometric ratio of 1:1 was pressed into the pellet using pellet pressure and kept in the quartz jacket. The maximum total weight of Co-As kept in the quartz jacket was 1 g. It was then evacuated on the vacuum line and sealed. Because As has very high vapor pressure, i.e., 28 atm at 800^{o}C, heating at a fast rate might cause the tube to explode. Also, CoAs is a congruently melting compound, so the heating was performed slowly. This was later kept in the outer quartz jacket and heated slowly to 300°C for 10hrs. The heating temperature was slowly increased at 1°C/min to 600°C and held at that temperature for 10hrs. The temperature was once again increased to 900°C and kept at that temperature for 10 hrs. The reaction was quenched in air. X-ray powder pure phase of Co-As was able obtained based on powder X-ray diffraction (Panalytical X'pert diffractometer).

The ternary compounds of $BaCo_2As_2$ were synthesized from solid state reaction of high purity of barium metal with X-ray powder pure Co-As precursor. A welded niobium tube containing barium and CoAs powder were placed in a fused silica jacket that was heated ultimately in the induction furnace at 40% voltage at the beginning and ends up with 33% voltage, i.e., at 950^{o}C after 4 hrs. The temperature was measured using infrared thermometer was 1200-1250°C. The reaction was quenched in air by shutting down the induction furnace. The tube was taken out and opened inside the glovebox and powder X-ray was taken. It was ground and pelletized and annealed at the 900^{o}C in the box furnace for 3 days. This was first slowly heated from 150^{o}C at 1°C/min

to 900° C, held at that temperature for 3 days and slowly cooled to 150° C at 1°C/min. Again powder X-Ray was taken and able to obtain pure phase of $BaCo_2As_2$. Annealing was done at 900°C for 3 days followed by slow cooling at 1°C/min and this is done to ensure the decomposition of the compound did not take place at that temperature.

The ternary compounds of KCo_2As_2 were synthesized from solid state reaction of high purity of potassium metal with X-Ray powder pure Co-As precursor. A welded niobium tube containing pure potassium and CoAs powder were placed in a fused evacuated silica jacket. The quartz ampoule with niobium tube inside containing stoichiometric potassium and CoAs powder was placed in the box furnace. Because the boiling point of potassium is 765°C, it was first slowly heated to 700° C for 10 hrs and the temperature was increased at 1 C/min to 750°C and held at that temperature for four days. It was further cooled slowly to 150° C at 1 C/min to 150° C. The sample was taken out and X-Ray powder was taken that matched well with the theoretical pattern. All the preparative manipulations were carried out in the purified argon filled glove box with total O_2 and H_2O level less than 1 ppm.

4.3 Crystallography of KCo_2As_2 and $BaCo_2As_2$

The single-crystal structure data have been reported for $BaCo_2As_2$[6] and KCo_2As_2.[7] Both of them crystallize in the $ThCr_2Si_2$ type, in tetragonal space group symmetry I4/mmm (No. 139: Z=2). The Co-As layers may be thought of as being built up by edge shared tetrahedrally coordinated $CoAs_4$ units. The stacking of Co_2As_2 layers are oriented such that distances between As-As layers are closest, though these are non-bonding. As described in the synthesis, $BaCo_2As_2$ and KCo_2As_2 were able to make

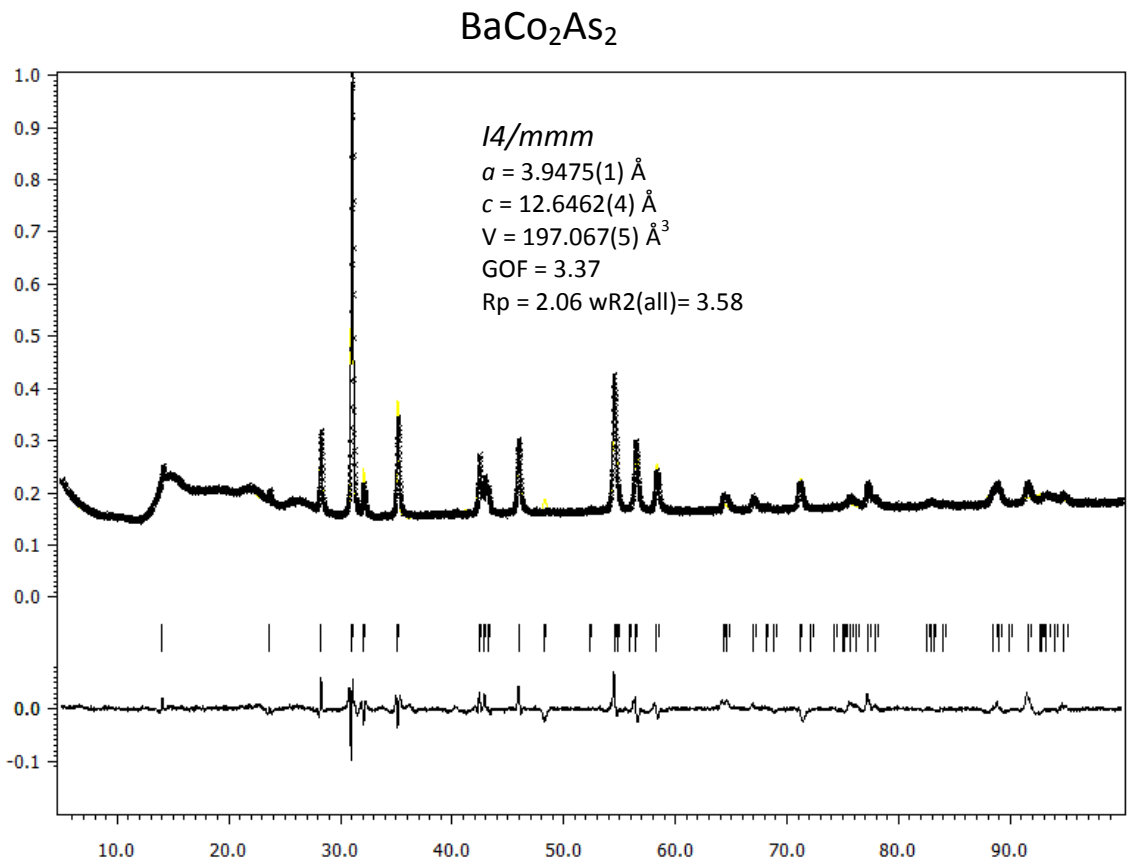

Figure 4.1: X-ray powder diffraction pattern of $BaCo_2As_2$. The lattice parameters were obtained from the Reitveld Refinement as implemented from the JANA 2006. The middle one shows the peak position while the one at the bottom shows the difference between the calculated and observed intensities.

KCo_2As_2

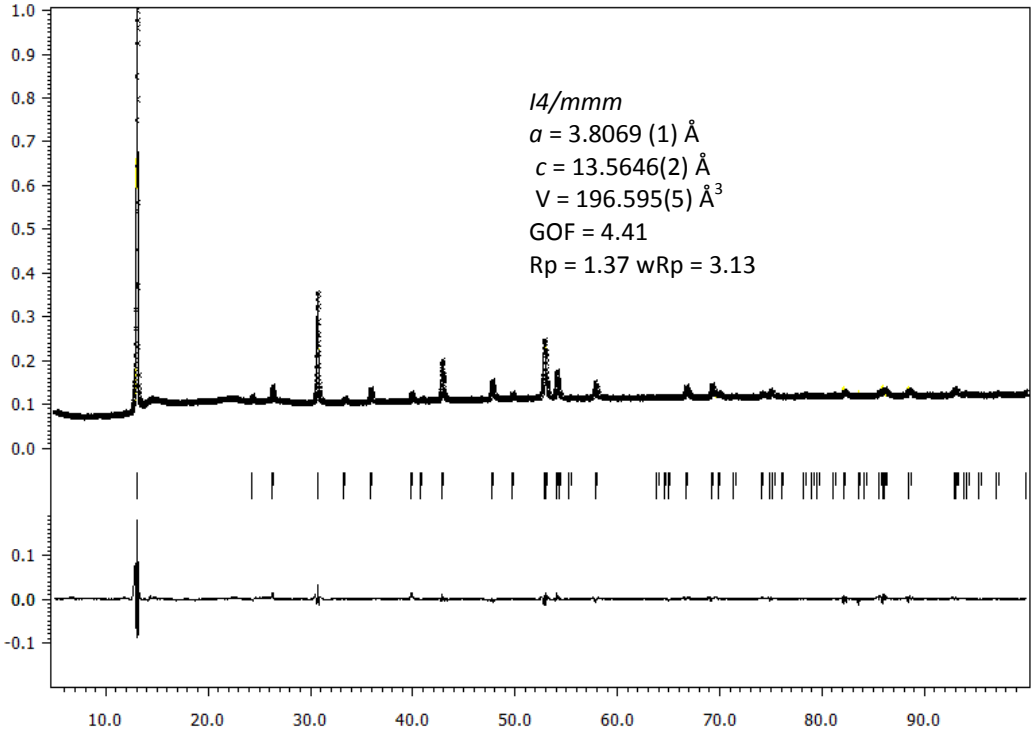

Figure 4.2: X-ray powder diffraction pattern of KCo_2As_2. The lattice parameters were obtained from the Rietveld refinement as implemented from the JANA 2006. The middle one shows the peak position while the one at the bottom shows the difference between the calculated and observed intensities.

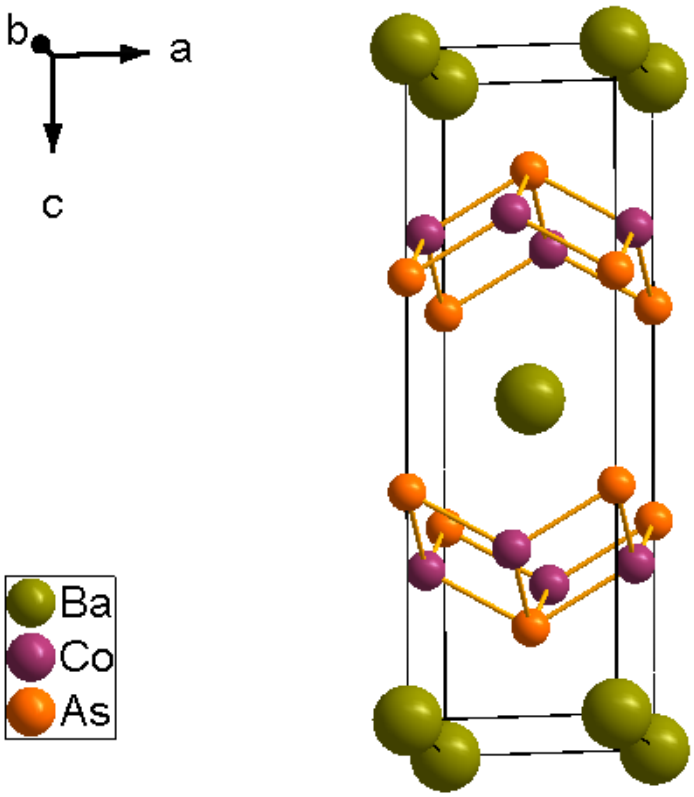

Figure 4.3: Unit cell of $BaCo_2As_2$ viewed along b. Co and As atoms form the layered network between which Ba atoms are placed.

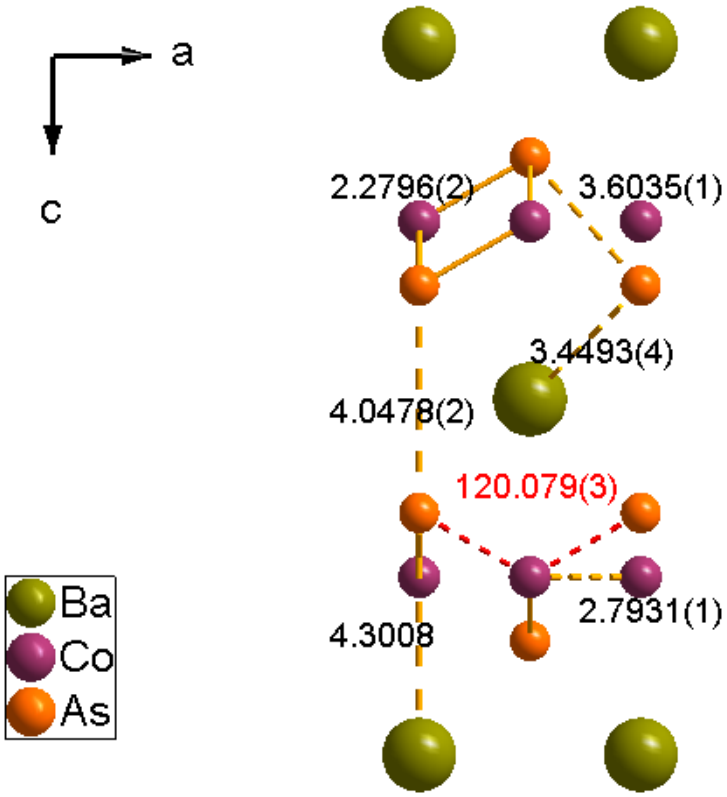

Figure 4.4: Arrangement of atoms showing bond distances (Å) and bond angle (^{o}) in $BaCo_2As_2$.

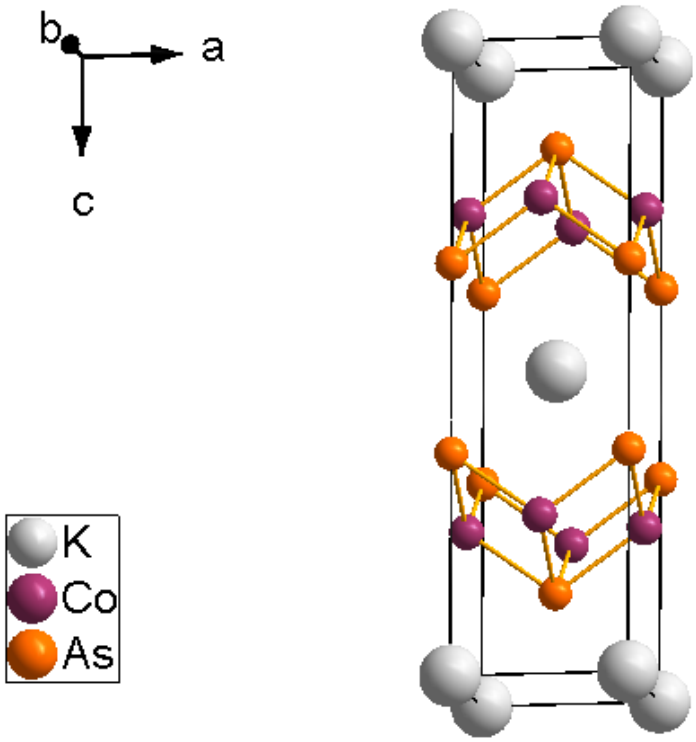

Figure 4.5: Unit cell of KCo_2As_2 viewed along b. Co and As atoms form the layered network between which K atoms are placed.

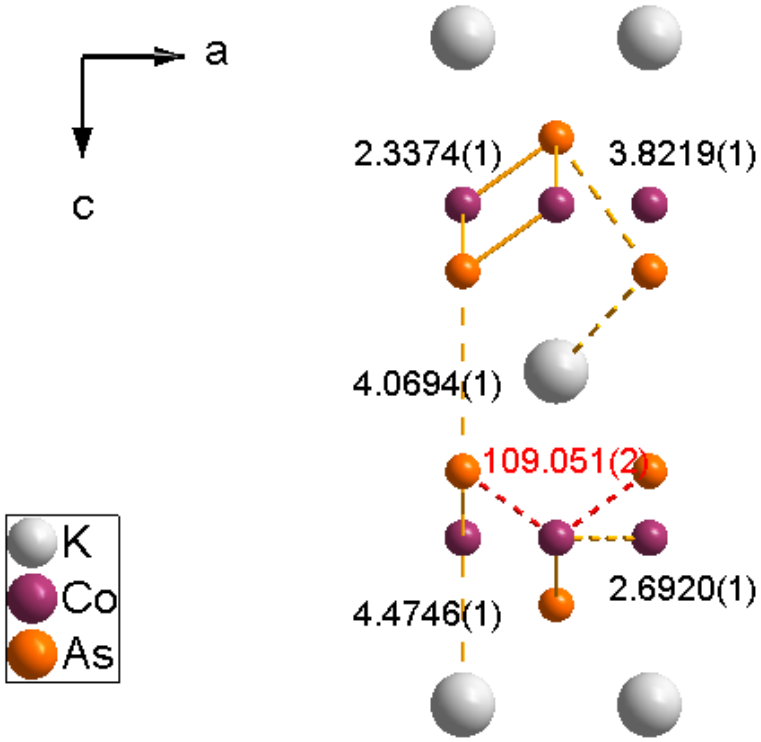

Figure 4.6: Arrangement of atoms showing bond distance (Å) and bond angles (^{o}) in KCo_2As_2.

(a)

	a (A)	*c* (A)	*c/a* ratio	T-X/Å	X-X/Å	X-T-X/^{o}	Volume (Å)^{3}
$BaCo_2As_2$	3.9475(1)	12.6462(4)	3.2043	2.2796	4.0478	120.079	197.062(5)
KCo_2As_2	3.8069(1)	13.5646(2)	3.5631	2.3374	4.0694	109.051	196.595(5)

(b)

	$BaCo_2As_2$	KCo_2As_2
Co-As(Å)	2.2796(1)	2.3374(1)
Co-Co(Å)	2.7931(1)	2.6920(1)
Co-Co(Å)	3.9500(1)	3.8070(2)
As-As(Å)	3.9500(1)	3.8070(2)
As-As(Å)	3.6035(1)	3.8219(1)
As-As(Interlayer(Å)	4.0478(2)	4.0694(1)
As-Co-As(^{o})	120.079	109.051

Table 4.1a: Unit cell parameters of $BaCo_2As_2$ and KCo_2As_2 and **b:** Relevant Bond distances and bond angles in $BaCo_2As_2$ and KCo_2As_2.

through the typical solid state reactions. The crystal structures were refined using the Rietveld refinement from JANA 2006. Figures 4.1 and 4.2 show the represented Rietveld refinements of $BaCo_2As_2$ and KCo_2As_2 respectively. Good data sets were collected. The refinements parameters are in well accepted limit with GOF around 4 and wR well below 4. The lattice parameters obtained are in close agreement with the published data. Table 4.1 shows the lattice parameters while the Table 4.2 presents the bond distances and bond angles of these compounds. The interlayer As-As distances in $BaCo_2As_2$ and KCo_2As_2 are almost the same as compared to the intralyer As-As distance. The interlayer distances are 4.0478Å and 4.0694Å in $BaCo_2As_2$ and KCo_2As_2 respectively. However, there is a considerable increase in the intralayer distance. And this is increased from 3.6035Å to 3.8219Å when Ba atoms are replaced by K atoms. This leads to the considerable decrease in the vertical angle As-Co-As (Table 4.1b) from 120^o to 109^o. This is quite interesting as the angle for the ideal tetrahedron is 109.5^o. It is observed that in KCo_2As_2, the lattice *a* is decreased and *c* is increased. Thus, the substitution with larger cations causes the elongation of the unit cell as well as the narrowing of the $CoAs_4$ tetrahedron. The Co_2As_2 layers of both the compounds are similar in their structures, though the layers are opened and oriented differently in terms of bond distances and bond angles.

4.4 Susceptibility measurements of $BaCo_2As_2$ and KCo_2As_2

The magnetic properties were performed on Quantum Design SQUID Magnetometer with the field up to 5T. The samples were loaded in gel capsule, sealed in the mason jar during transfer, and then quickly moved into SQUID. Zero field-cooled

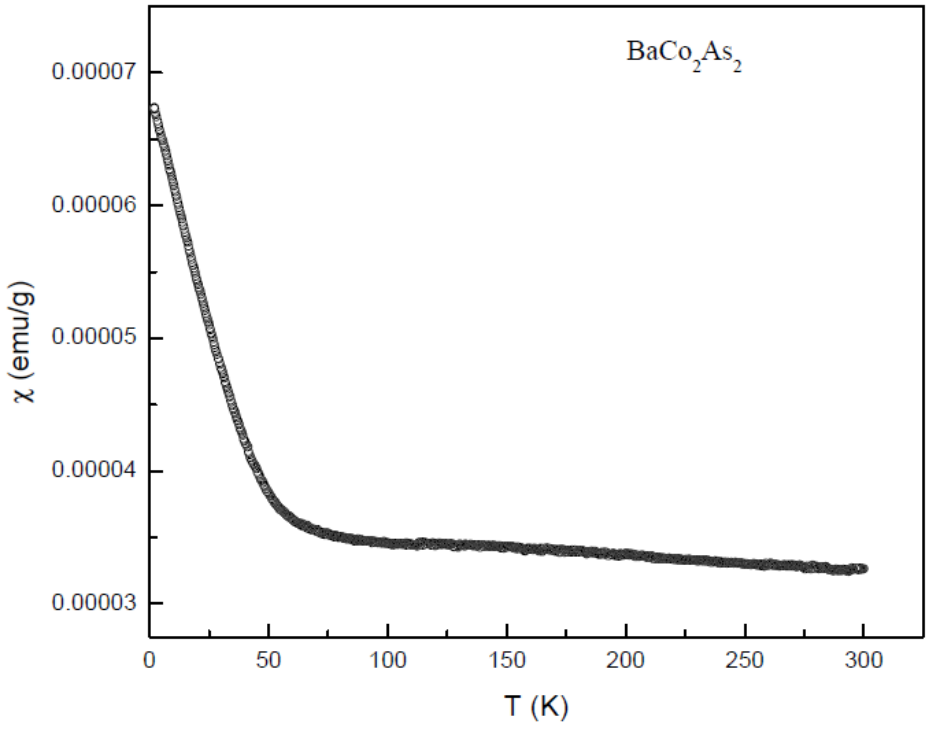

Figure 4.7: Magnetic susceptibility as a function of temperature for $BaCo_2As_2$

Figure 4.7 shows the magnetic susceptibility as a function of temperature for $BaCo_2As_2$. The susceptibility shows Curie like behavior. However, at high temperature the susceptibility is not small which might be contribution from free electrons Pauli paramagnetism.

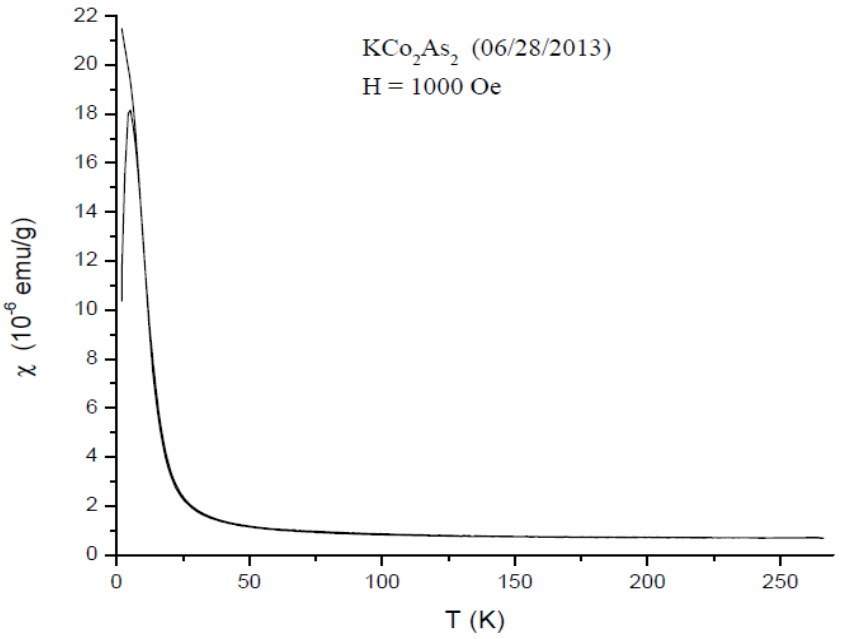

Figure 4.8: Magnetic susceptibility as a function of temperature for KCo_2As_2

Figure 4.8 shows the susceptibility versus temperature for KCo_2As_2. It increases at low temperature and the zero field and field cool curve splits at 15 K. This magnetic transition is due to weak ferromagnetism.

ZFC) and field cooled (FC) measurements were performed. Since ACo_2As_2 (A=K, Ba) are all moisture sensitive, precaution were taken to avoid possible moisture attack.

Conclusions

In conclusion, $BaCo_2As_2$ and KCo_2As_2 that crystallize with $ThCr_2Si_2$ structure type were successfully prepared through solid state synthesis. The magnetic measurement shows $BaCo_2As_2$ to be the pauli-paramagnetic while KCo_2As_2 to be weakly ferromagnetic.

References

(1) Hoffmann, R.; Zheng, C. *J. Phys. Chem.* **1985**, *89*, 4175-4181.

(2) Johrendt, D.; Felser, C; Jepsen, O.; Andersen, O. K.; Mewis, A.; Rouxel, J. *J. Solid State Chem.* **1997,***130*, 254-265.

(3) Francois, M.; Venturini, G.; Mareche, J. F.; Malaman, B.; Roques, B. *J. Less-Common Metals* **1985,***113*, 231-237'.

(4) Jeitschko, W.; Glaum, R.; Boonk, L. *J. Solid State Chem.* **1987,** *69*, 93- 100.

(5) Hirjak, M.; Lejay, P.; Chevalier, B.; Etourneau, J.; Hagenmuller, P. *J. Less-Common Metals* **1985,** *105*, 139-148.

(6) Pfisterer, M; Nagorsen, G. Zeitschrift fuer Naturforschung, Tel B. Anorganishe Chemie, Organische Chemie (33, 1978-41, 1986) **1980**, *35*, 703-704

(7) Rozsa, S.; Schuster, H. U. Zeitschrift fuer Naturforschung, Tel B. Anorganishe Chemie, Organische Chemie (33, 1978-41, 1986) **1981**, *36*, 1668-1670

Chapter 5

$K_xBa_{1-x}Co_2As_2$ Compounds

5.1 Introduction

In the previous chapter, structure and properties of ternary Co-As with $ThCr_2Si_2$-type and related structures were explored, revealing structural features. Here, in this chapter, the focus is shifted to more precisely to potassium doped $BaCo_2As_2$. The appearance of weak itinerant ferromagnetism in $SrCoGe_{1-x}P_x$ with the breaking of dimer[1] also opens up the avenue for CoAs based compounds as well as various doped compounds on the various sites. With this in mind, we attempt to dope the K into the Ba sites. Here, the diffraction pattern, structure, shifting of hkl values and the variations of the lattice parameters were studied.

5.2 Experimental Section

Reagents: The following reagents were used as received and were stored and handled under argon atmosphere in glovebox: K (99.95% metal basis, Alfa Aesar), Co (powder, 99.98% Alfa Aesar), Ba (dendrites, 99.99% Aldrich), As (lumps, 99.99% Alfa Aesar).

Synthesis: KCo_2As_2 and $BaCo_2As_2$ adopted the same $ThCr_2Si_2$-type tetragonal structure type, thus it was easier to make $K_xBa_{1-x}Co_2As_2$ samples by annealing the stoichiometric amounts of the ternary compounds. The ternary compounds of KCo_2As_2 and $BaCo_2As_2$ were synthesized from solid state reaction of high purity of alkali metal or alkaline earth metal with X-ray powder pure CoAs precursor as described in the previous chapter.

Polycrystalline samples of $K_xBa_{1-x}Co_2As_2$ were prepared from stoichiometric amounts of the ternary end members of KCo_2As_2 and $BaCo_2As_2$. In total, seven different samples were loaded. Before the loading of the ternary end products, the samples were thoroughly mixed, ground, compressed into pellet and placed in the Nb containers. The containers were thereafter welded and were subsequently placed into a fused silica jacket that was sealed under vacuum. The assembly was kept in the box furnace and annealed at 900°C for 3 days. This was followed by slow cooling at 1^oC/min to 150^oC. The high phase purity of the ternary compounds guarantees the exceptional quality of the solid solutions and the precise control of the chemical compositions. All the preparative manipulations were carried out in a purified argon filled glove box with total O_2 and H_2O level less than 0.1 ppm. The niobium tubes and quarts tube were cleaned and dried in the oven prior to use to prevent any possible contamination. The phase purity of the polycrystalline samples were investigated by powder X-ray diffraction (Panalytical X'pert Diffractometer).

5.3 Crystal Structure and Lattice Parameters:

The X-ray powder diffraction data of all the samples were able to be indexed. All of these are found to be crystallized in the $ThCr_2Si_2$-type structure with the space group I4/mmm and Z=2. Good data were able to be collected and lattice parameters refinements of the all the samples were performed using JANA 2006 program. The representatives of the le Bail profile refinements patterns are listed in the Figures 5.1 to 5.7. The difference between the calculated and observed peaks is also presented in these Figures. Also, the lattice parameters of these samples obtained after profile refinements were provided.

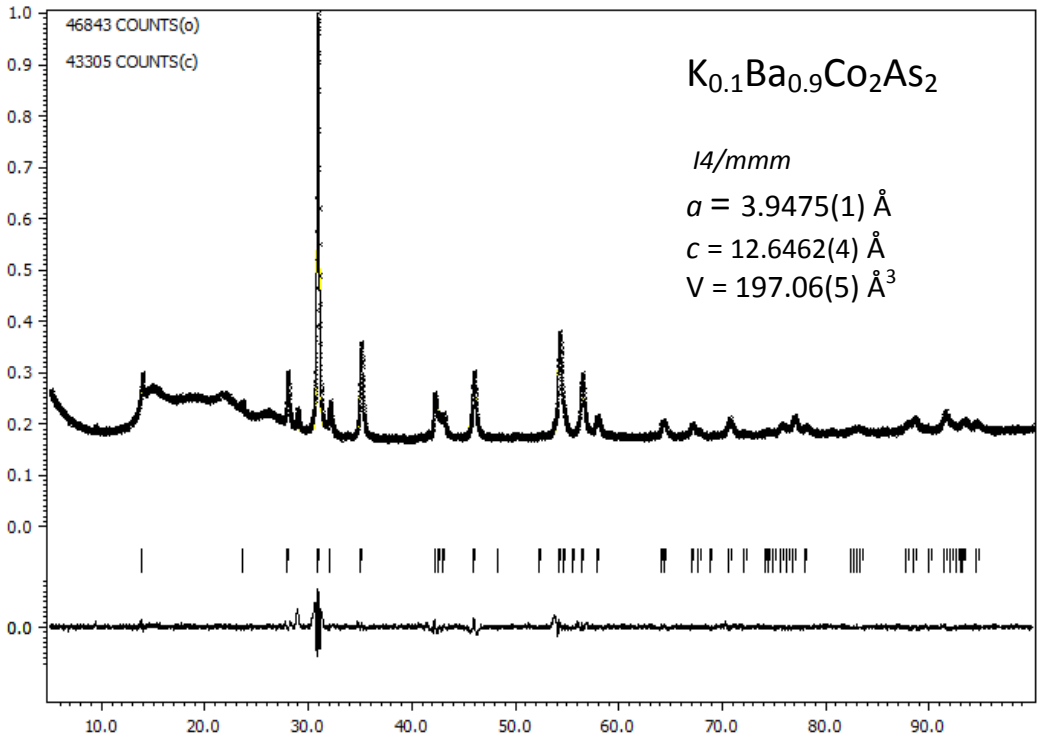

Figure 5.1: Powder diffraction pattern of $K_{0.1}Ba_{0.9}Co_2As_2$ as obtained from le Bail profile refinement using JANA 2006. The middle one shows the peak positions while the lower one shows the difference between the observed and calculated peaks.

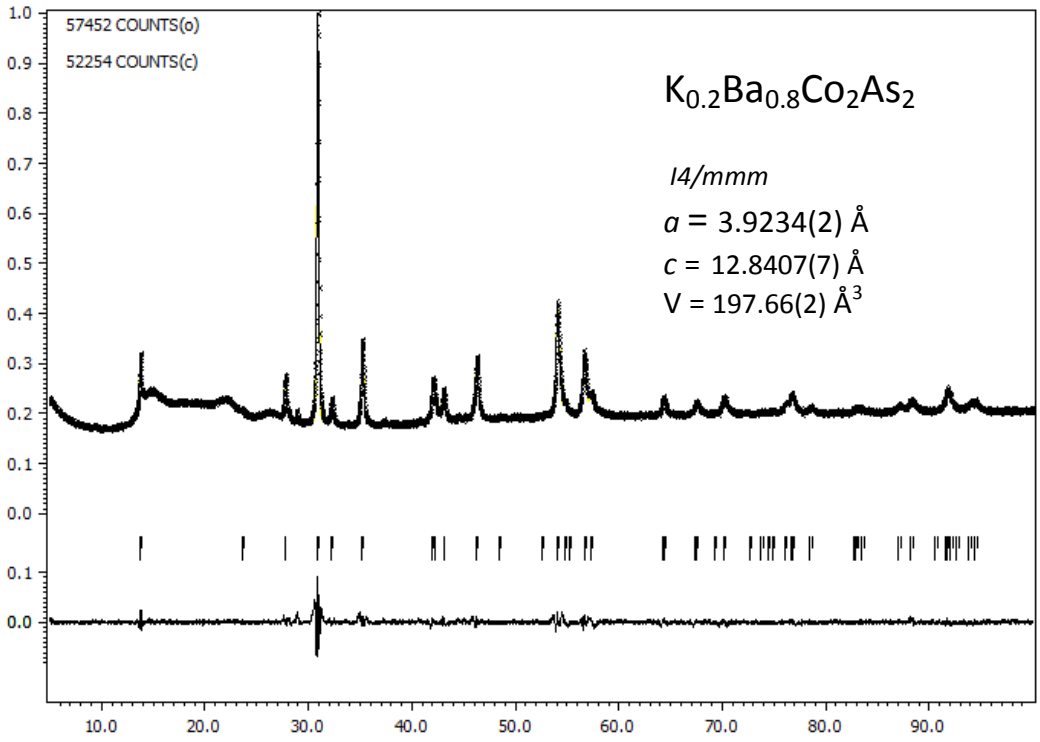

Figure 5.2: Powder diffraction pattern of $K_{0.2}Ba_{0.8}Co_2As_2$ as obtained from le Bail profile refinement using JANA 2006. The middle one shows the peak positions while the lower one shows the difference between the observed and calculated peaks.

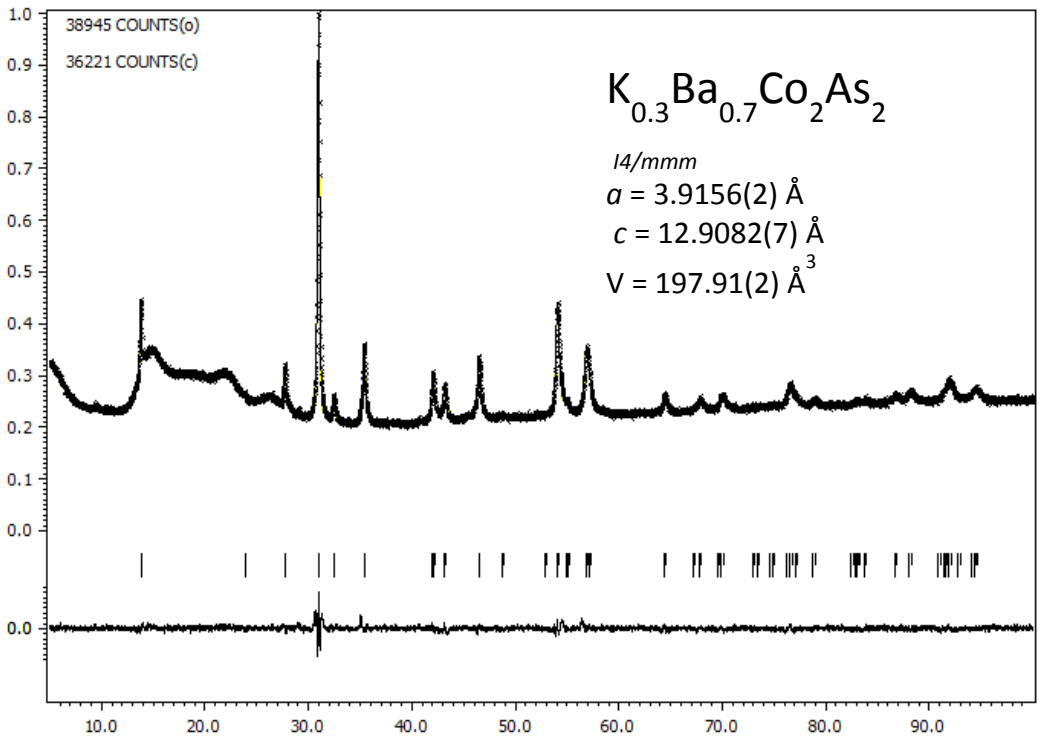

Figure 5.3: Powder diffraction pattern of $K_{0.3}Ba_{0.7}Co_2As_2$ as obtained from le Bail profile refinement using JANA 2006. The middle one shows the peak positions while the lower one shows the difference between the observed and calculated peaks.

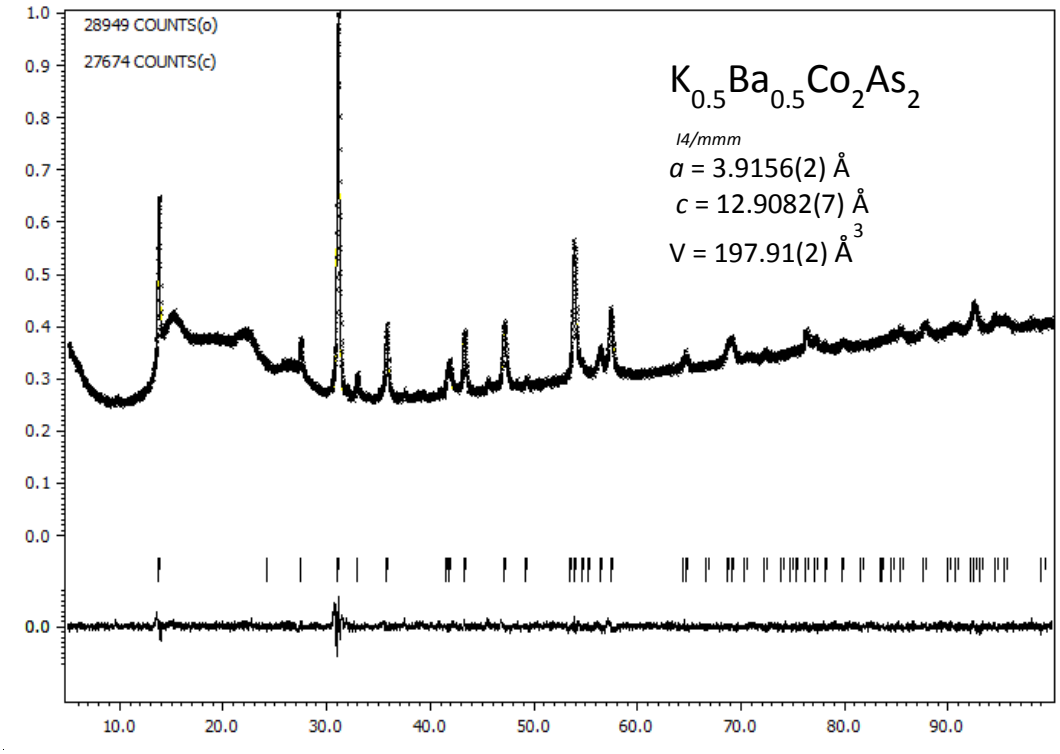

Figure 5.4: Powder diffraction pattern of $K_{0.5}Ba_{0.5}Co_2As_2$ as obtained from le Bail profile refinement using JANA 2006. The middle one shows the peak positions while the lower one shows the difference between the observed and calculated peaks.

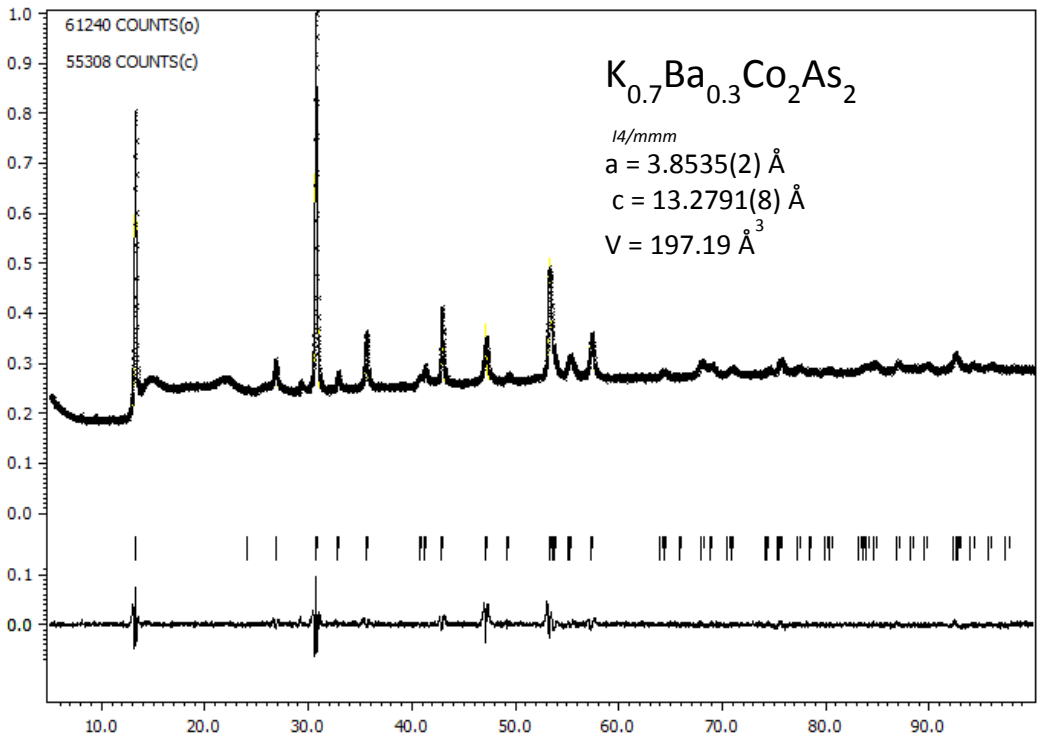

Figure 5.5: Powder diffraction pattern of $K_{0.7}Ba_{0.3}Co_2As_2$ as obtained from le Bail profile refinement using JANA 2006. The middle one shows the peak positions while the lower one shows the difference between the observed and calculated peaks.

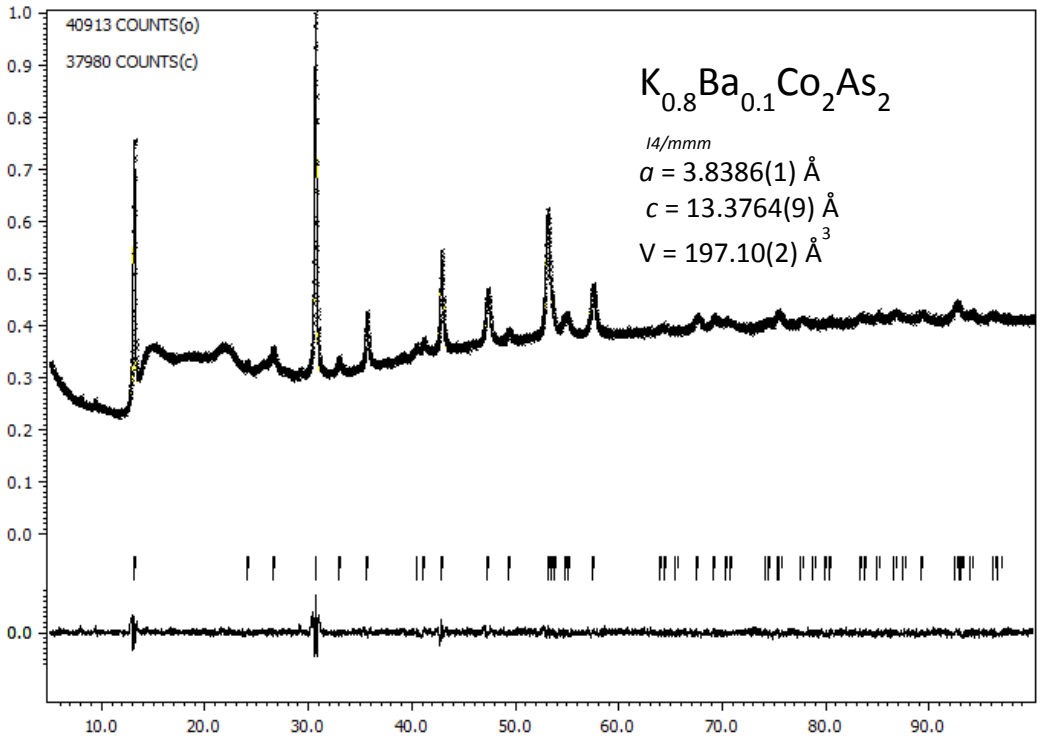

Figure 5.6: Powder diffraction pattern of $K_{0.8}Ba_{0.2}Co_2As_2$ as obtained from le Bail profile refinement using JANA 2006. The middle one shows the peak positions while the lower one shows the difference between the observed and calculated peaks.

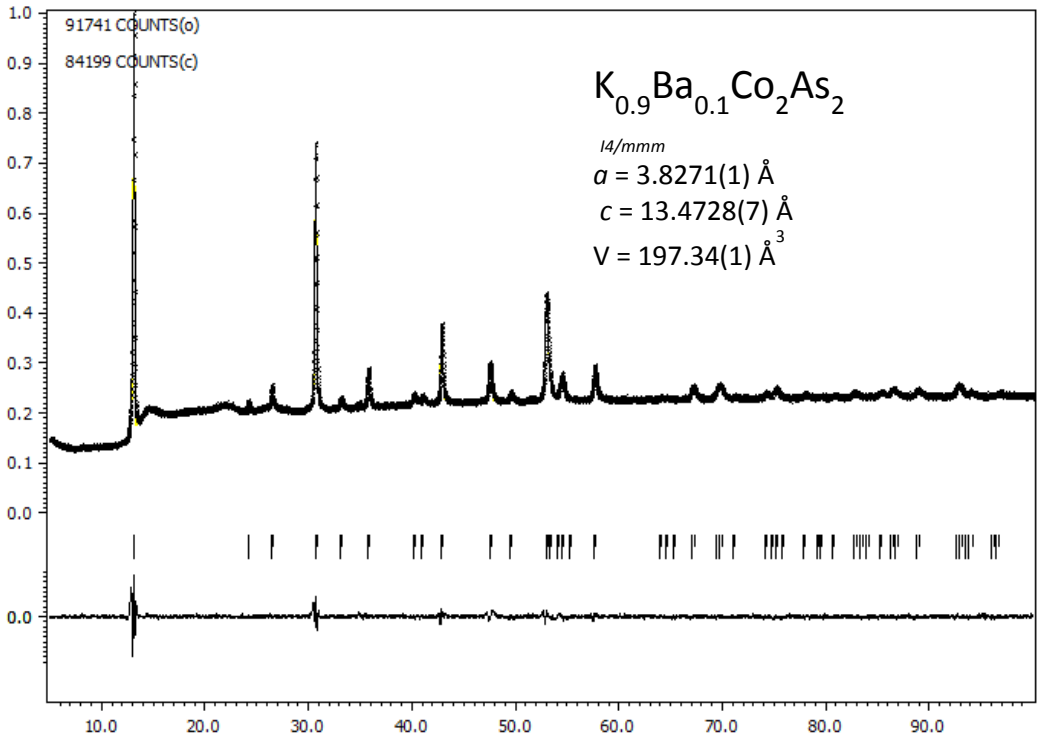

Figure 5.7: Powder diffraction pattern of $K_{0.9}Ba_{0.8}Co_2As_2$ as obtained from le Bail profile refinement using JANA 2006. The middle one shows the peak positions while the lower one shows the difference between the observed and calculated peaks.

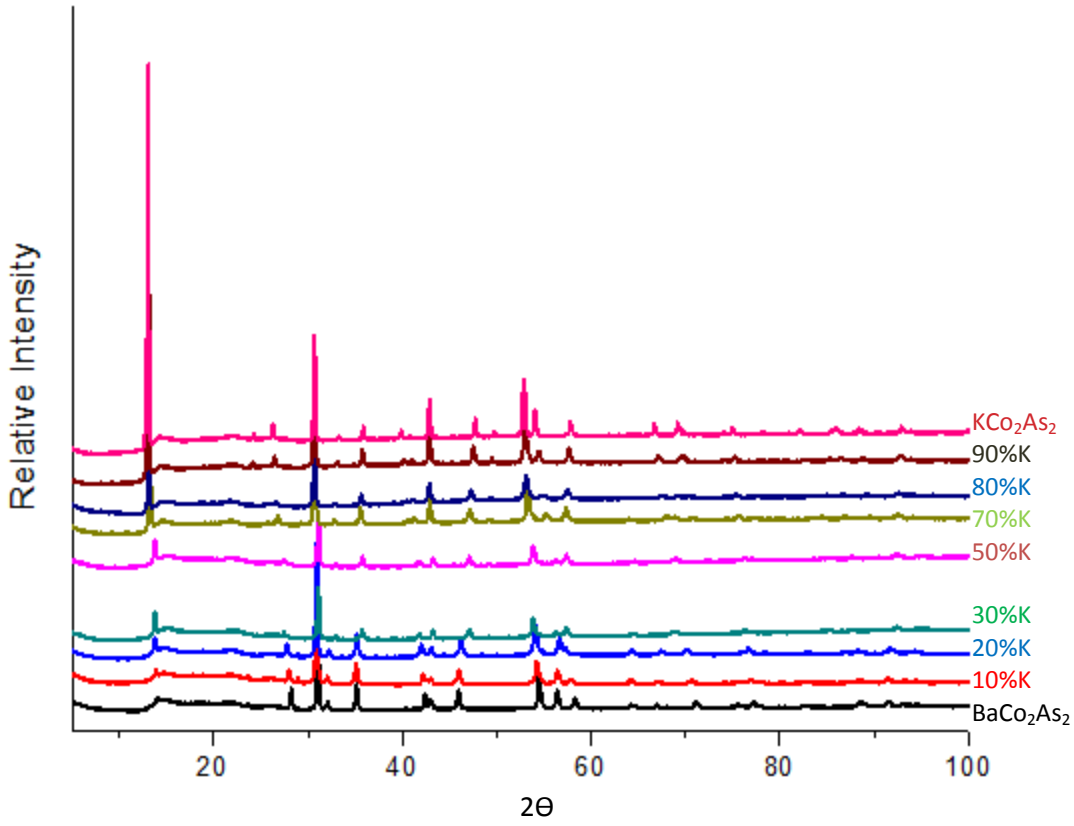

Figure 5.8: Comparison of X-ray powder diffractions of doped samples $Ba_xK_{1-x}Co_2As_2$ and the end members; $BaCo_2As_2$ and KCo_2As_2 plotted against 2 theta.

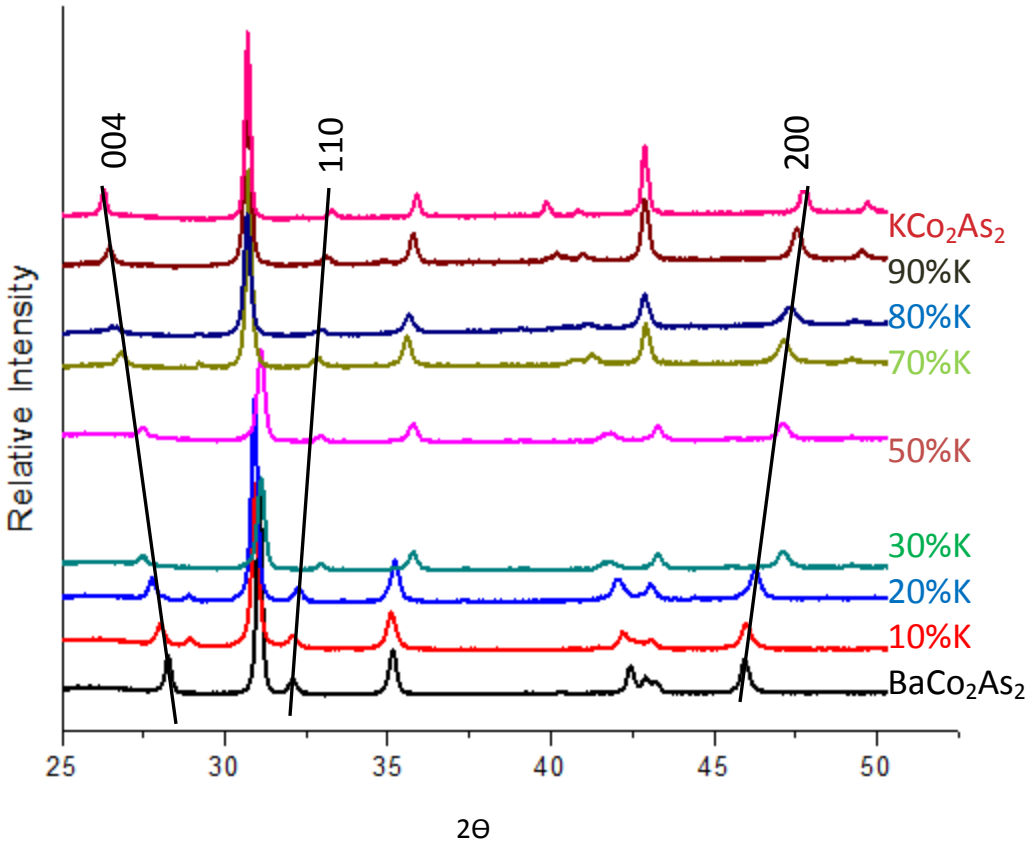

Figure 5.9: Magnified portion of Powder diffraction showing shifting of peaks for various hkl values. Straight lines are shown for 004, 110 and 200 hkl peaks. The shifts in these peaks are linear except for the 30% doped sample.

Figure 5.8 shows the X-Ray powder diffraction patterns of ternary end members: $BaCo_2As_2$ and KCo_2As_2 as well as those of doped samples. The bottom one belongs to the $BaCo_2As_2$ phase while the one at the top represents the KCo_2As_2 phase. In between are the seven different doped potassium phases. There is a systematic increase in potassium content as we go from bottom to top. The x-axis shows the 2Θ values ranged from 5^o to 100^o while the y-axis shows the relative intensity. These are plotted using the Origin Pro 8.

Figure 5.9 is the magnified portion of the Figure 5.2 plotted between 25 and 50 degrees of 2Θ values. After indexing all the doped samples as well as the pure samples, it can be seen the peaks at 004 are shifted to the left (lower angle) while the peaks at 110 and 200 are shifted to the right (higher angle). This gives us an indication that the lattice *c* is increased while lattice *a* is decreased. And these changes are consistent as we go to from barium rich phase to potassium rich phase. Therefore, it gives us an indication that lattice *a* will be decreased while the lattice *c* will be increased from barium rich to barium poor phase. And these changes are consistent with the lattice parameters obtained from le Bail profile refinement.

From the Table 5.1, it can be observed that with the increase in the potassium content, *a* is decreased while *c* is increased. This is quite evident as Ba atom is being substituted by larger potassium atom. Increase in *c* is quite pronounced compared to decrease in *a*. This results in the increase in *c/a* ratio as more potassium is being substituted by more barium atoms. However, the volume remains almost constant throughout the doped samples.

	***a* (Å)**	***c* (Å)**	***c/a* ratio**	**V(Å^3)**
$BaCo_2As_2$	3.9475(1)	12.6462(4)	3.2024	197.06(5)
$Ba_{0.9}K_{0.1}Co_2As_2$	3.9440(2)	12.7335(7)	3.2286	198.07(2)
$Ba_{0.8}K_{0.2}Co_2As_2$	3.9234(2)	12.8407(7)	3.2726	197.66(2)
$Ba_{0.7}K_{0.3}Co_2As_2$	3.9156(2)	12.9082(7)	3.2965	197.91(2)
$Ba_{0.5}K_{0.5}Co_2As_2$	3.8768(1)	13.1099(6)	3.3807	197.04(1)
$Ba_{0.3}K_{0.7}Co_2As_2$	3.8535(2)	13.2791(8)	3.4459	197.19(2)
$Ba_{0.2}K_{0.8}Co_2As_2$	3.8386(1)	13.3764(9)	3.4847	197.10(2)
$Ba_{0.1}K_{0.8}Co_2As_2$	3.8271(1)	13.4728(7)	3.5203	197.34(1)
KCo_2As_2	3.8069(1)	13.5646(2)	3.5605	196.59(5)

Table 5.1: Lattice parameters *a* and *c* of the $K_xBa_{1-x}Co_2As_2$ samples. The *c*/*a* ratio and volume are also given.

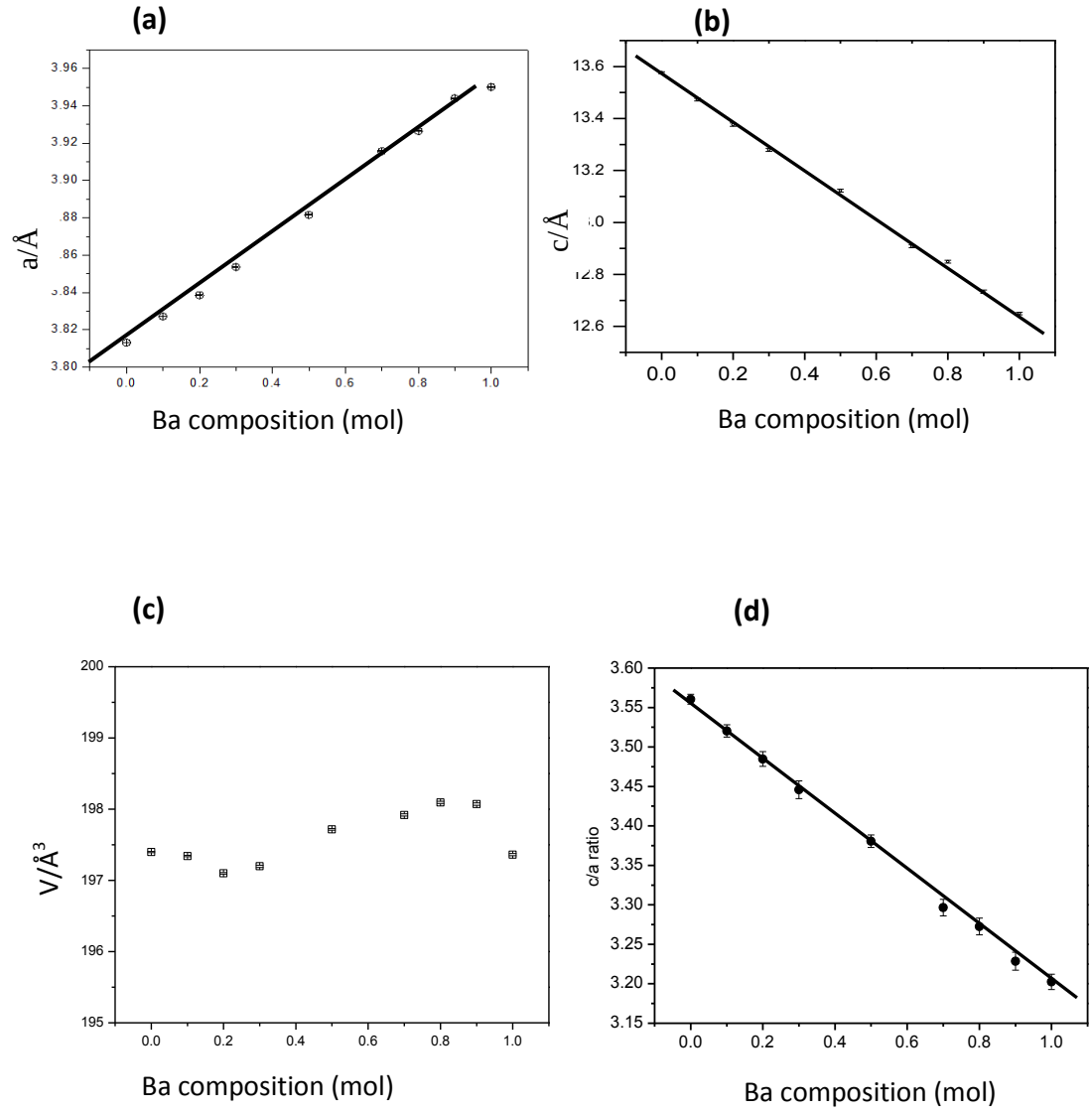

Figure 5.10 (a): Plot of lattice parameter *a* vs Ba compositon (**b):** Plot of lattice parameter *c* vs Ba composition **(c):** Plot of *c/a* vs Ba compositon and **(d):** Plot of Volume vs Ba composition. The error bars along y axis are also shown. The top left one shows the linear increase in *a* with the increase in the Ba composition. The top right shows the linear decrease in c with increase in Ba composition. The bottom right shows linear decrease in *c*/*a* ratio. The bottom left shows the change in volume with the increase in Ba composition.

5.4 Discussions and Conclusion

The change in the lattice parameters and *c*/*a* ratio will certainly affect the bonding and structure of this system. When replacing the smaller Ba atoms with bigger K atoms, the larger K atoms result in the slightly longer As-As interlayer distance. It greatly increases the intralyer As-As distance. The Figure 5.10 shows there is linear increase in lattice a as Ba atoms are substituted by K atoms. In the Figure 5.5, it can be observed that there is linear increase in lattice c as smaller Ba atoms are replaced by the larger K atoms. Also, there is linear increase in *c*/*a* ratio. This means that elongation along c is pronounced compared to decrease in lattice *a*. We can see that the $CoAs_4$ tetrahedra in $BaCo_2As_2$ is not perfect tetrahedra, the doping effect of K into Ba sites might cause the geometry change of $CoAs_4$ tetrahedra from distorted tetrahedral to perfect tetrahedra in pure KCo_2As_2. From the Figure 5.10, it is evident that the volume remains constant throughout the doping samples. From the plot and the powder pattern, it is evident that the doping of K into the Ba site is quite successful; the measurements of these samples can be done in order to understand its underlying properties.

References

(1) Jia, S.; Jiramongkolchai, P.;Suchomel, M.R.; Toby, B.H.;Checkelsky, J.G.; Ong N.P.; Cava, R.J. *Nature* **2011**, *7*, 207-210.